

**Measuring transversity in polarized p+p  
collisions with di-hadron correlations at  
 $\sqrt{s} = 200$  GeV at the STAR experiment**

Keith Landry

today

## **Abstract**

The transversity distribution  $h_1(x)$  of a transversely polarized proton describes the fraction of partons with polarization parallel to the parent proton, carrying a momentum fraction  $x$  of the parent proton. This distribution is fundamental for our understanding of the proton spin structure but still very much unknown for values of  $x$  larger than about 0.15. In order to understand transversity better, we study transversely spin-polarized proton collisions at STAR, as polarized p+p collisions at RHIC can access this  $x$  region and, with a higher scale and transverse momentum, probe a different kinematic regime than SIDIS. We find sizable spin asymmetries in di-hadron correlations, which can be used to directly probe the transversity distribution of quarks inside protons because they arise from a transversely spin polarized quark fragmenting into two hadrons by the Interference Fragmentation Function. This talk will present precision measurements of di-hadron correlations which from the STAR experiment at RHIC, which are sensitive to transversity.

# Contents

<b>List of Figures</b>	<b>5</b>
<b>List of Tables</b>	<b>7</b>
<b>1 Introduction</b>	<b>10</b>
1.1 ?history of matter/elementary physics/quarks? . . . . .	10
1.2 parton model/QCD? . . . . .	11
1.3 parton distributions . . . . .	11
1.4 Quark Fragmentation . . . . .	15
<b>2 Experimental Landscape</b>	<b>17</b>
2.1 Unpolarized Distribution Function . . . . .	17
2.2 The Helicity Distribution Funtion . . . . .	17
2.3 Measuring the Interference Fragmentation Function at Belle . . . . .	18
<b>3 RHIC and The STAR Experiment</b>	<b>20</b>
3.1 The RHIC complex . . . . .	20
3.2 The STAR Detector . . . . .	23
3.3 STAR triggers . . . . .	34
3.4 Particle Identification . . . . .	34

<b>4 Theoretical background</b>	<b>35</b>
<b>5 2006 analysis and sim</b>	<b>39</b>
<b>6 2012 IFF</b>	<b>44</b>
6.1 Data Set and Cuts? . . . . .	44
6.2 particle Identification . . . . .	44
6.3 Finding $\pi^+\pi^-$ Pairs . . . . .	44
6.4 Pair Distributions . . . . .	50
6.5 Determining the angles . . . . .	50
6.6 Calculating The Asymmetry . . . . .	50
<b>7 Results</b>	<b>55</b>
7.1 One Dimensional Kinematic Binning . . . . .	55
7.2 Check For False Asymmetries . . . . .	55
7.3 Two Dimensional Kinematic Binning . . . . .	60
7.4 Kaon Pion Pairs . . . . .	63
<b>8 Trigger Bias</b>	<b>67</b>
<b>9 discussion</b>	<b>69</b>
<b>Bibliography</b>	<b>70</b>

# List of Figures

1.1 Visual representation of unpolarized, helicity, and transversity distribution functions . . . . .	13
1.2 Current knowlege of parton distribution functions . . . . .	14
1.3 Interference Fragmentation Function . . . . .	15
1.4 Collins Fragmentation Function . . . . .	16
2.1 HERMES results for helicity distribution function . . . . .	18
2.2 Asymmetry seen in $e^-e^+$ annihilation at Belle . . . . .	19
3.1 The RHIC complex . . . . .	22
3.2 Spin flip by Siberian Snake . . . . .	23
3.3 STAR Time Projection Chamber . . . . .	24
3.4 Anode sector of STAR TPC . . . . .	26
3.5 Ionization energy loss in TPC gas . . . . .	27
3.6 Barrel Electromagnetic Calorimeter . . . . .	29
3.7 Barrel Electromagnetic Calorimeter 2 . . . . .	30
3.8 Shower Maximum Detector cross sectional view . . . . .	31
3.9 Spatial reconstruction in the SMD . . . . .	31
3.10 pVPD detector element . . . . .	32

3.11	pVPD Assembly	33
3.12	STAR Time of Flight System	33
4.1	Angles $\phi_S$ and $\phi_R$	38
5.1	$AUT$ vs Invariant Mass in 2006 data set	40
5.2	$AUT$ for different opening angles	41
5.3	$AUT$ vs $\eta^{\pi^+\pi^-}$ in 2006 data set	42
5.4	Partonic momentum fraction in 2006 simulation forward and backward $\pi^+\pi^-$ pair	43
6.1	Schematic of Analysis	45
6.2	Ionization energy loss in TPC gas on log scale	46
6.3	$n_\sigma(\pi)$ distribution and tripple Gaussian fit	47
6.4	Contamination of pion sample	48
6.5	Radius cut	49
6.6	Sinusoid modulation of $\pi^+\pi^-$ pair produciton and fit for 9 $P_T^{\pi^+\pi^-}$ bins	53
6.7	Sinusoid modulation of $\pi^+\pi^-$ pair produciton and fit for 9 $P_T^{\pi^+\pi^-}$ bins	54
7.1	Need name here	57
7.2	Asymmetry in $\pi^+\pi^-$ pair with randomly assigned charges	58
7.3	Asymmetry in $\pi^+\pi^-$ pairs when proton spin is randomly assigned	59
7.4	Asymmetry vs $\eta^{\pi^+\pi^-}$ and $P_T^{\pi^+\pi^-}$ 2D binning	61
7.5	Three different views of $\eta^{\pi^+\pi^-}$ , $P_T^{\pi^+\pi^-}$ 2D binning	62
7.8	Asymmetry vs Invariant Mass for Kaon Pion Pairs	66
8.1	Trigger bias toward higher momentum fraction $x$ events	68

## **List of Tables**

# Acronyms

<b>IFF</b>	interference fragmentation function
<b>QCD</b>	quantum chromo dynamics
<b>STAR</b>	Solenoid Tracker at RHIC
<b>RHIC</b>	Relativistic Heavy Ion Collider
<b>DIS</b>	deep inelastic scattering
<b>pdf</b>	parton distribution function
<b>HERMES</b>	?????
<b>SLAC</b>	Stanford Linear Accelerator Center
<b>Belle</b>	??????
<b>BNL</b>	Brookhaven National Laboratory
<b>AGS</b>	Alternating Gradient Synchrotron
<b>LINAC</b>	
<b>OPPIS</b>	optically pumped proton ion source
<b>TPC</b>	Time Projection Chamber

<b>BEMC</b>	Barrel Electromagnetic Calorimeter
<b>PMT</b>	photomultiplier tube
<b>SMD</b>	Shower Maximum detector
<b>ToF</b>	Time of Flight
<b>VPD</b>	
<b>BBC</b>	Beam Beam Counter
<b>JP</b>	Jet Patch trigger
<b>HT</b>	High Tower trigger
<b>UU</b>	unpolarized-unpolarized
<b>UT</b>	unpolarized-transversely polarized

# 1 Introduction

## 1.1 ?history of matter/elementary physics/quarks?

We know a lot about the internal structure of the proton. We have known for a quite a while that the proton is made up of even smaller particles. In 1968 deep inelastic scattering experiments at the Stanford Linear Accelerator (SLAC) showed the first evidence the proton was made up of quarks, and in 1979 the Positron-Electron Tandem Ring Accelerator (PETRA) produced evidence of gluons inside the proton. We know that the intrinsic angular momentum (or spin) of the proton is  $\frac{1}{2}$ , however, we are not quite sure why. Since the proton is made up of quarks and gluons, it seems like the spin of the proton needs to come from these constituents, so we look at the parton kinematics inside the proton. This is described to leading order by a set of three distributions - the unpolarized distribution  $f_1(x)$ , the helicity distribution function  $g_1(x)$ , and the transversity distribution function  $h_1(x)$ .

The unpolarized distribution function describes the probability of finding a parton with momentum fraction  $x$  inside of the proton. This is known quite well from deep inelastic scattering (DIS). The helicity distribution function is similar. It also describes the probability to find a parton with momentum fraction  $x$  inside the proton but with a difference. The proton in this case has its spin direction aligned with its momentum, and the proba-

bility is the difference in finding the quark's spin aligned vs anti-aligned with the proton's spin. Like the unpolarized distribution, this too is known quite well from DIS experiments.

We know a lot about the structure of the proton. Thanks to something we know it consists of partons (quarks and gluons). We know that the valence quarks are uud. other stuff. We know it's intrinsic angular momentum (or spin) is  $\frac{1}{2}$ . However we still don't know why it's spin is always  $\frac{1}{2}$ . The naive explanation is that it comes directly from the spin of the two up quarks and the down quark that make up the proton. However this does not totally account for the proton's spin. The spin of gluons and the orbital angular momentum of both the quarks and gluons needs to be taken into account.

## 1.2 parton model/QCD?

## 1.3 parton distributions

In order to understand the spin of the proton, we need to look to the parton distribution functions. This set of three functions tell the complete story of parton kinematics inside the proton at leading order. The first parton distribution function called the unpolarized distribution function  $f_1(x)$  is well known from deep inelastic scattering (DIS). It tells the probability of finding a parton with momentum fraction  $x$  inside of the proton. That is if the proton has a momentum  $\vec{P}$ ,  $f_1(x)$  tells the probability of finding a parton with momentum  $x\vec{P}$ . The second parton distribution function is also fairly well known from DIS. It is called the helicity distribution function and denoted  $g_1(x)$ . This distribution function tells the difference in probability of finding a parton whose spin is aligned with the proton's spin with momentum fraction  $x$  and of finding a parton whose spin is anti aligned with the proton's spin with momentum fraction  $x$  inside a proton whose spin is aligned with its direction of motion. The final parton distribution function is the transversity

Distribution function  $h_1(x)$ . This is very similar to the helicity distribution function. The only difference being the proton spin is perpendicular to the direction of motion for the transversity distribution function instead of aligned with it. These parton distribution functions are represented pictorially in figure 1.1.

The unpolarized and helicity distributions, which can be seen in figure ??, are known accurately for different Bjorken  $x$  and momentum transfer of the hard scattering process  $Q^2$ . On the other hand, the transversity distribution, which can also be seen in figure ??, is not well known at all event for just  $x$ . This is because the transversity distribution function is chiral odd while the unpolarized and helicity distributions are chiral even. This allows the unpolarized and helicity distribution to be accessed through DIS. Since all observables must be chiral even, the transversity distribution can not be accessed through DIS. It has to be paired with another chiral odd quantity to make a chiral even observable.  
j??DO I DO SOMETHING HERE SHOWING THAT IT'S CHIRAL ODD WITH SOME PICTURES AND STUFF???

Several chiral odd candidates to pair with the transversity distribution function have been considered. One such candidate is a transversely polarized Drell-Yan process. This is not ideal because the cross section is small and involves an antiquark transversity distribution as well. jSTUFF ABOUT OTHER POSSIBLE CANDIDATESj The candidates which makes the most sense are chiral odd quark fragmentation functions.

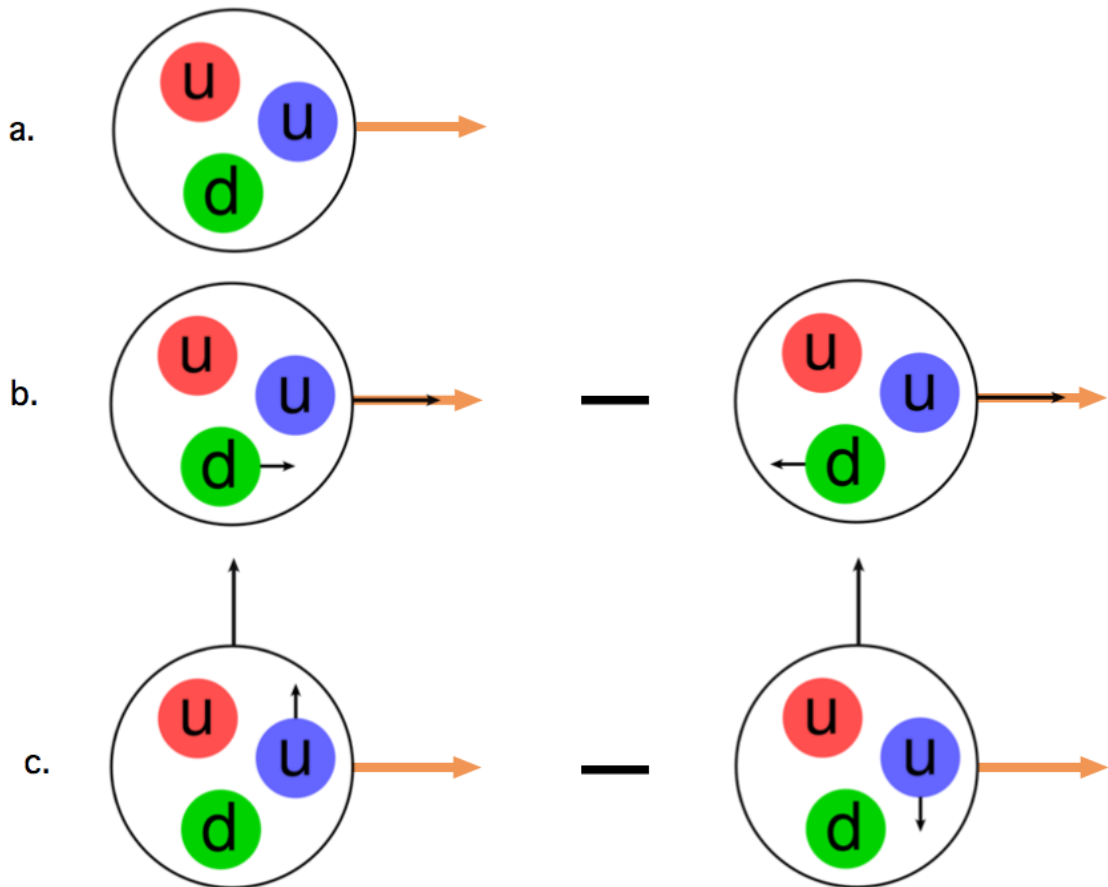


Figure 1.1: a. Unpolarized distribution function  $f_1(x)$

b. Helicity distribution function  $g_1(x)$

c. Transversity distribution function  $h_1(x)$

Black arrows denote proton or paron spin, orange arrow denotes direction of proton momentum.

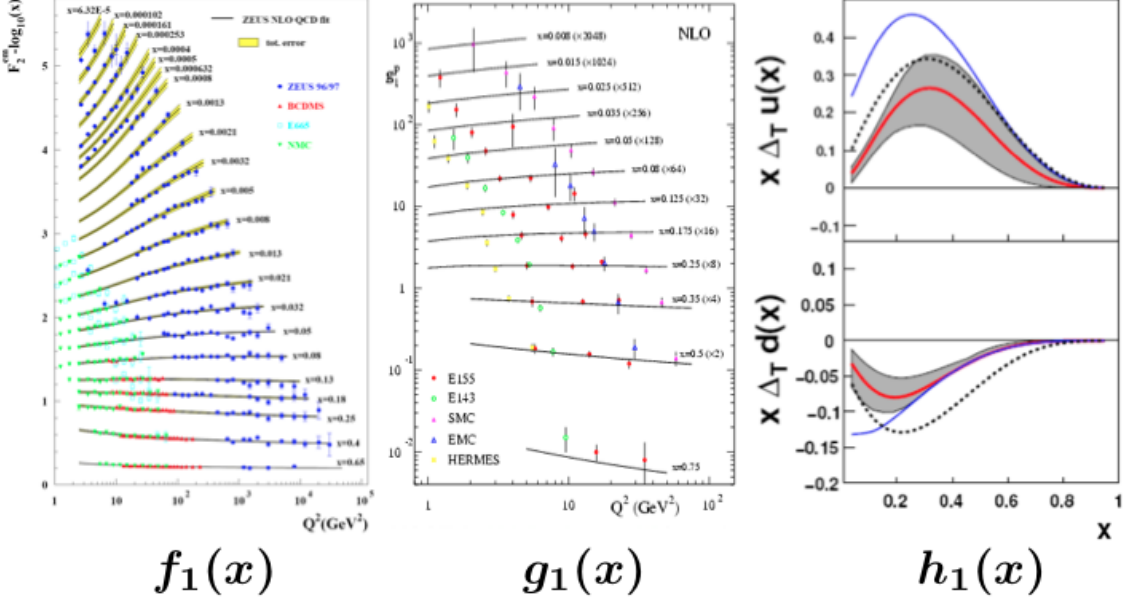


Figure 1.2: Left and center pannels show the unpolarized and helicity distribution functions as a function of momentum transfer  $Q^2$  for different values of the momentum fraction  $x$ . The right pannel shows out best knowlege of the transversity distribution function for the up quark (top) and the down quark (bottom) vs momentum fraction  $x$ . The grey band shows the uncertainty of the transversity distribution function. The Blue line is a more leanient uncertainty. The dotted line shows the helicity distribution function for the up and down quarks.

|ADD REFERENCES TO THE PLOTS|

## 1.4 Quark Fragmentation

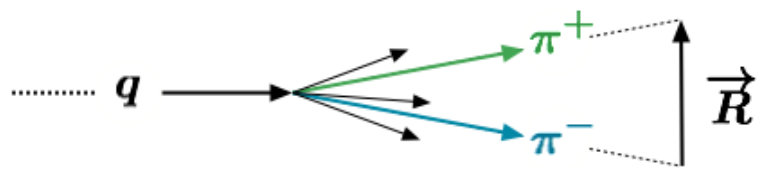


Figure 1.3: an outgoing quark fragments into a  $\pi^+\pi^-$  pair. This is described by the Interference Fragmentation Function (IFF). The Vector  $\vec{R}$  gives the orientation of the pair.

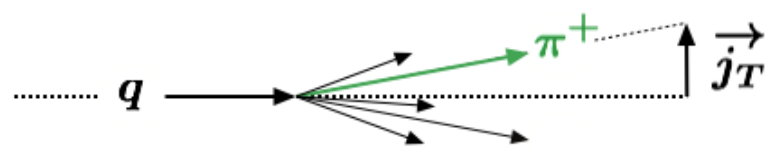


Figure 1.4: an outgoing quark fragments into a  $\pi^+$  (or  $\pi^-$ ). This is described by the collins fragmentation function.  $\vec{j}_T$  is the component of the pion momentum transvers to the jet axis.

## 2 Experimental Landscape

Before getting into my analysis, I would like to start by acknowledging the experiments that have impacted our knowledge of the parton distribution functions.

### 2.1 Unpolarized Distribution Function

### 2.2 The Helicity Distribution Function

The helicity distribution  $g_1(x)$  has been measured accurately by multiple collaborations. In 1997 the HERMES collaboration measured the helicity distribution using a combination of inclusive and semi-inclusive lepton-nucleon deep inelastic scattering data. ?? The data was taken with 27.6GeV longitudinally polarised positron beam scattering off a longitudinally polarized hydrogen gas target. They constructed an asymmetry  $A_{||}$  in the number of scattered positrons.

$$A_{||} = \frac{N^- L^+ - N^+ L^-}{N^- L_P^+ + N^+ L_P^-} \quad (2.1)$$

Where  $N^+(N^-)$  is the number of positrons scattered when the target spin is parallel(antiparallel) to the positron beam spin. The luminosities are  $L^+, L^-$  when the target spin is parallel or antiparallel with the beam spin, while  $L_P^+, L_P^-$  are weighted luminosities. The helicity distribution function was extracted based on its relation to this asymmetry.

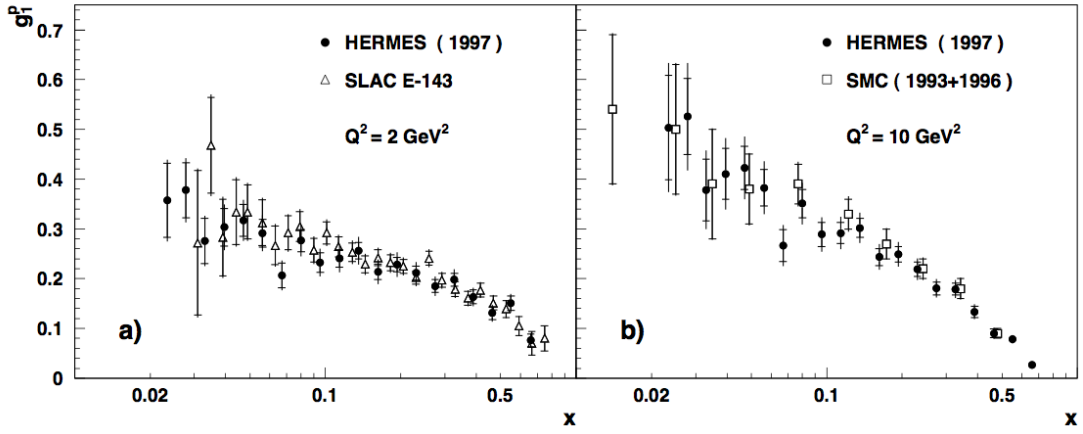


Figure 2.1: The helicity distribution as a function of momentum fraction  $x$  for  $Q^2 = 2$   $\text{GeV}^2$  and  $10 \text{ GeV}^2$ .

$$\frac{g_1}{F_1} = \frac{1}{1 + \gamma^2} \left[ \frac{A_{||}}{D} + (\gamma - \eta) A_2 \right] \quad (2.2)$$

Hermes is not the only collaboration to extract the helicity distribution. The Hermes data along with other experiments data is shown in figure 2.1.

## 2.3 Measuring the Interference Fragmentation Function at Belle

In our experiment, transversity only shows up as a convolution with the interference fragmentation function  $h_1 H_1^\triangleleft$ . In order to isolate transversity in our data we need to know how the interference fragmentation function behaves. Luckily for us Belle already did this work. They performed an electron positron annihilation experiment detecting back to back  $\pi^+ \pi^-$  pairs. A relative angle between the two pions was measured and a modulation  $a_{12}$  of the number of back to back pairs found at different values of the relative angle was seen. This modulation is related to two IFFs.

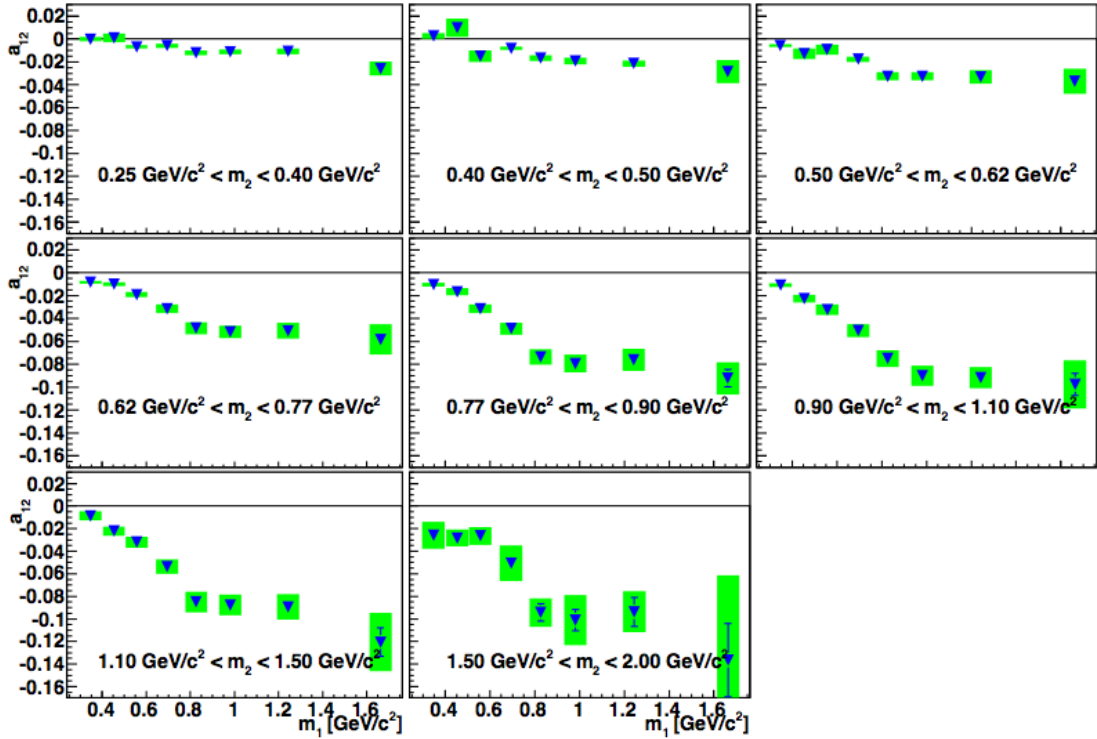


Figure 2.2: Asymmetry in the number of back to back pion pairs seen at Belle plotted vs the invariant mass.

$$a_{12} \propto \frac{1}{2} \frac{\sin^2 \theta}{1 + \cos^2 \theta} \left[ \sum_{q,\bar{q}} e_q^2 z_1^2 z_2^2 H_1^{\triangleleft q}(z_1, m_1^2) H_1^{\triangleleft \bar{q}}(z_2, m_2^2) \right]^{-1} \times \left[ \sum_{q,\bar{q}} e_q^2 z_1^2 z_2^2 D^q(z_1, m_1^2) D^{\bar{q}}(z_2, m_2^2) \right]^{-1} \quad (2.3)$$

Here  $\theta$  is the polar angle defined between the beam axis and the reference axis,  $D^q$  is the unpolarized equivalent of the IFF,  $z_{1(2)}$  is the energy fraction pion pair 1(2) has, and  $m_{1(2)}$  is the invariant mass of pair 1(2). The people at Belle reported the modulation  $a_{12}$  for different  $z_1, z_2$  bins as well as different  $m_1, m_2$  bins for different quark flavors. The modulation  $a_{12}$  is shown in figure 2.2 plotted versus the invariant mass. With this data, Courtoy et al were able to extract the Interference Fragmentation Function.[5]

## 3 RHIC and The STAR Experiment

### 3.1 The RHIC complex

The Relativistic Heavy Ion Collider, located at Brookhaven Nation Lab, is one of the only places in the world that allows for polarized proton collisions, yet is also able to collide heavy nuclei as the name suggests. It actually is composed of a chain of accelerators which boost the energy in steps before finally injecting the particles into the large ring of RHIC. For heavy nuclei are delivered to the Booster Synchrotron where they are accelerated to 95MeV per nucleon. After which they are transferred to the Alternating Gradient Synchrotron (AGS). Here they re-bunched into four bunches and accelerated to 10.8 GeV per nucleon, at which point they are injected into the RHIC ring and accelerated to their final energy. The highest energy RHIC can accommodate for heavy ions is 100 GeV per nucleon. The story for protons is a little different. They are injected already spin polarized into the Booster Synchrotron from an older LINAC accelerator. In order to keep the spin polarization for the proton beam, special magnets called Siberian Snakes are used. These magnets flip the proton spin by 180 degrees. From this point they are accelerated in the Booster and AGS before being injected into the RHIC storage ring. Here they are accelerated up to a maximum 250 GeV. The RHIC storage ring itself actually consists of two independent rings 3.8 km in circumference. This allows for the collisions of different

species. The independent rings intersect at six locations. the STAR detector is located at one such intersection points. [*RHIC project overview*]

As acceleration of polarized protons in a circular accelerator cause resonances which act to depolarize the beam. Special magnets called Siberian Snakes are used to overcome these depolarizing resonances. The roll of the Siberian Snakes rotate the proton spin. If the spin rotation from the Siberian Snakes is much larger than that of the depolarizing resonances, the beam polarization is kept intact. In the RHIC ring, this is achieved with Siberian Snakes which rotate the proton spin by 180 degrees. The lower energy of the AGS calls for only partial Siberian Snakes which rotate less than 180 degrees, but still enough to maintain beam polarization. [10] Each Siberian Snake consists of 4 superconducting helical dipole magnets. Along with the Siberian Snakes, spin rotators are located at the six interaction points. These allow for the proton spin to be rotated from the transverse plane to the longitudinal plane. [10]

Polarized protons start out as polarized  $H^-$  ions produced from an optically pumped proton ion source (OPPIS). This source produces  $9 \times 10^{11}$  polarized  $H^-$  ions per  $300\mu s$  pulse. These polarized ions are then accelerated to 200 MeV in the LINAC. They are then stripped of the electrons and injected into the Booster where they are further accelerated to 10.5 GeV. From here they are sent to the AGS and accelerated to 25 GeV. The final step is a transfer to RHIC for acceleration to a maximum of 25 GeV and storage. [10]

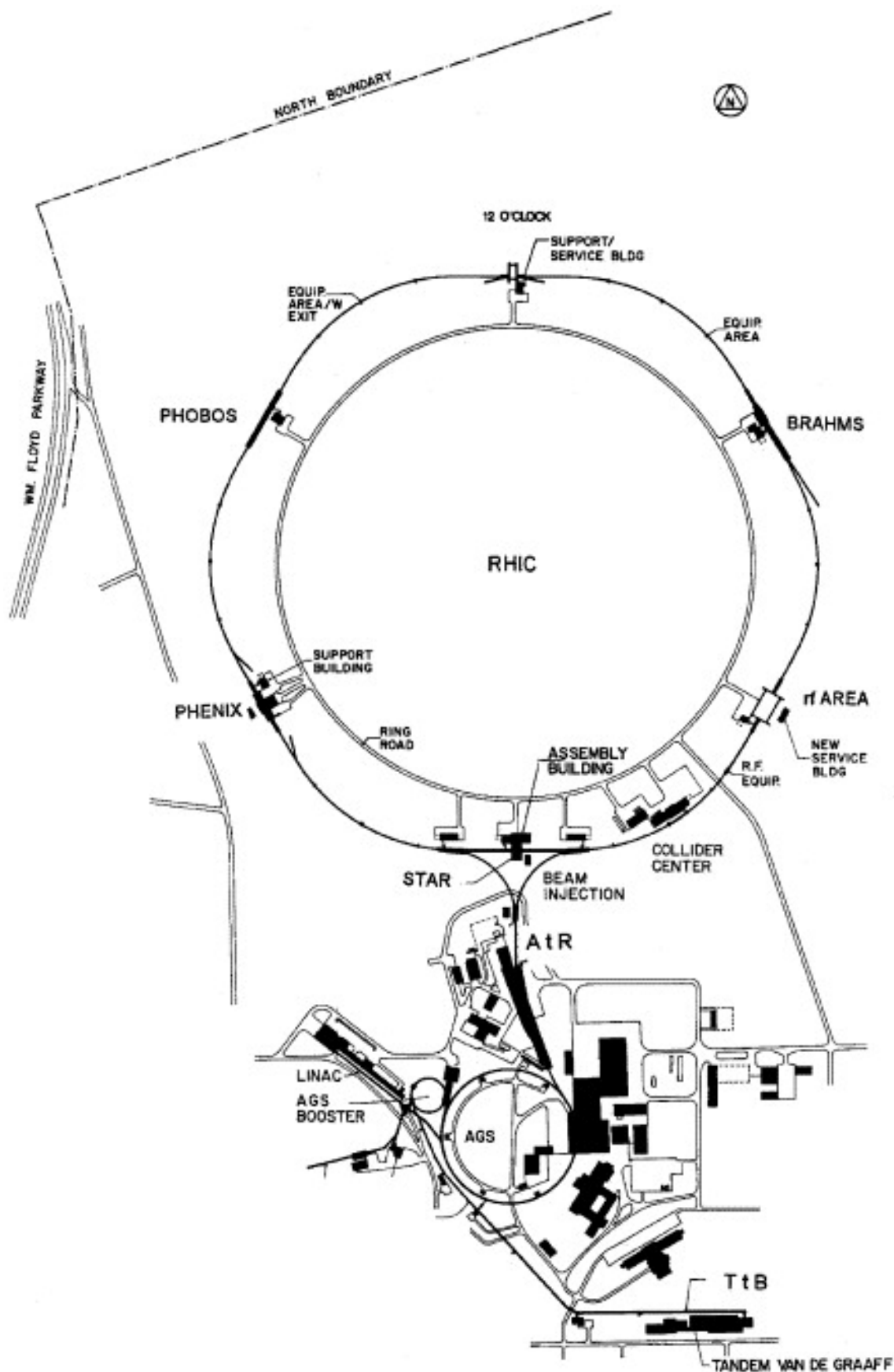


Figure 3.1

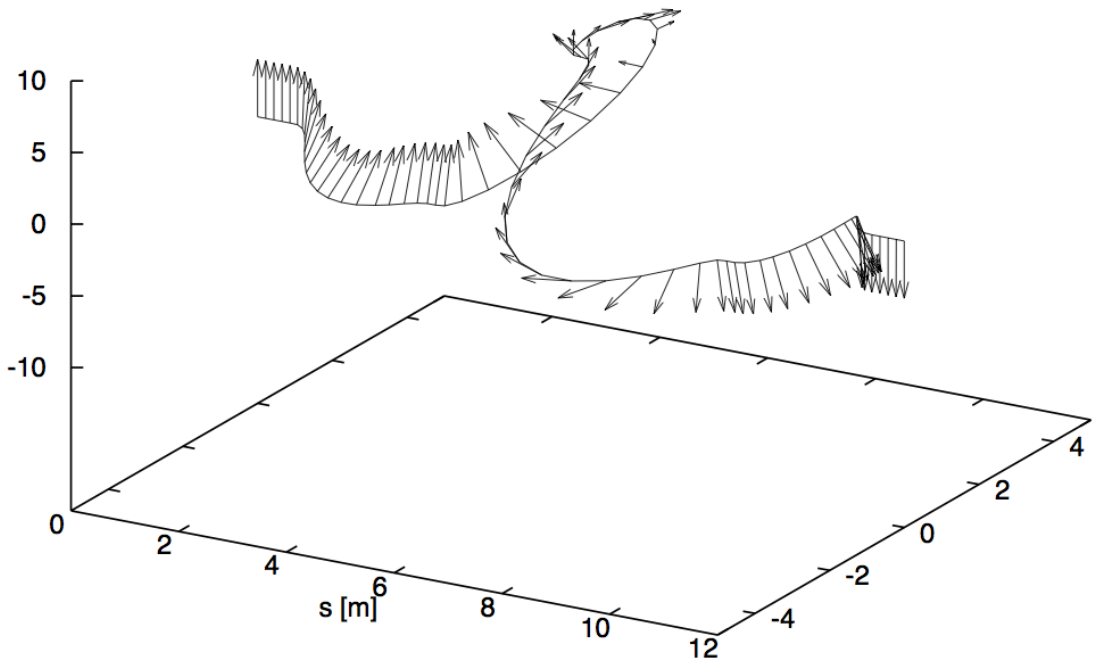


Figure 3.2: 180 degree proton spin flip by Siberian Snake

### 3.2 The STAR Detector

The Solinoid Tracker at RHIC (STAR) is bullshit about the history and stuff.

#### Time Projection Chamber

One of the key detectors of STAR is the Time Projection Chamber (TPC). It is tasked with tracking particles, measuring momenta, and detecting  $dE/dx$  energy loss to aid in particle identification. As a track traverses the TPC it ionizes the gas inside. The track also bends due to STAR's magnetic field an amount proportional with the velocity of the track. These allow for the tracking of particles, the measurement of particle momenta, and the  $dE/dx$  ionization energy loss aids in particle identification.

The TPC is the large cylindrical gas chamber covering  $\pm 1.8$  units of pseudorapidity around the interaction point. It's filled with a mixture of 10% methane and 90% argon at

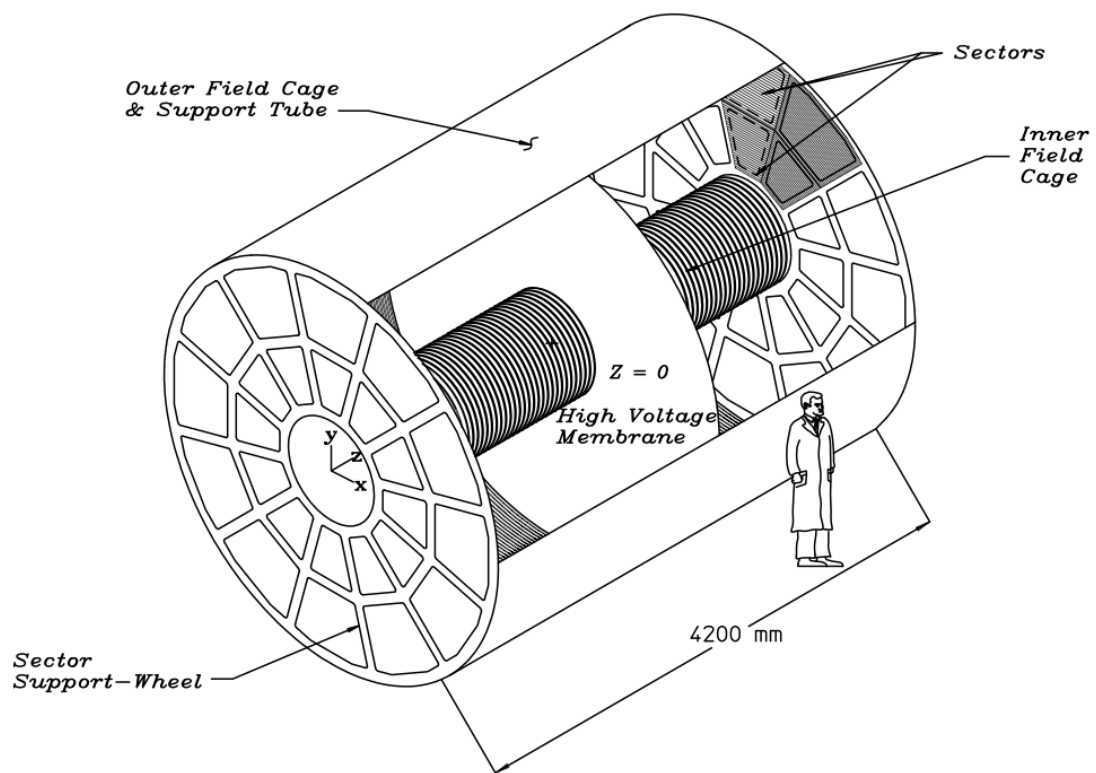


Figure 3.3: STAR Time Projection Chamber

a pressure of 2mbar above atmospheric pressure. As a charged particle passes through the TPC, the gas is ionized. Electrons from the ionization drift to the end caps of the TPC under a uniform electric field of about 135 V/cm where they are reconstructed.

At the center of the TPC is a central membrane which splits the TPC in two halves. This membrane is kept at 28 kV while the two end caps are at ground. A field cage is located around the TPC to create 182 equipotential slices in the TPC. This set up allows for a very uniform electric field to be kept.

A mixture of 10% methane and 90% argon is chosen for the TPC gas due to its fast drift velocity. This drift velocity also peaks at the operating electric field (135 V/cm) making it relatively unaffected by subtle fluctuations in the electric field.

The TPC gas drift velocity is calibrated with a laser system. Thirty six aluminum plates are positioned on either side of the central membrane and are illuminated with an ultraviolet laser. This causes photo-ejection of electrons which drift to the end caps where they are read. The position of the aluminum plates are known with such precision that the time it takes the ejected electrons to reach the end cap readouts as well as the position they reach can be used for calibration.

The end cap is equipped with 12 modular sectors arranged in a circle. These sectors are arranged like a clock with only 3mm separating them. Each sector, shown in figure 3.4, has a grid of readout pads and a wire proportional chamber consisting of three wire girds; a gated grid, a shield (or ground) grid and an anode grid. The gated grid is required to keep boundary conditions with the central membrane and field cage in order to achieve the uniform electric field, and is thus arranged to do so. The anode wire plane is made up of  $20\mu$  wires aligned radially around the sector. This is to achieve maximum precision of the measurement of momenta from high momentum (straight) tracks. The anode grid is completed by wires in the other direction separated by 4 mm.

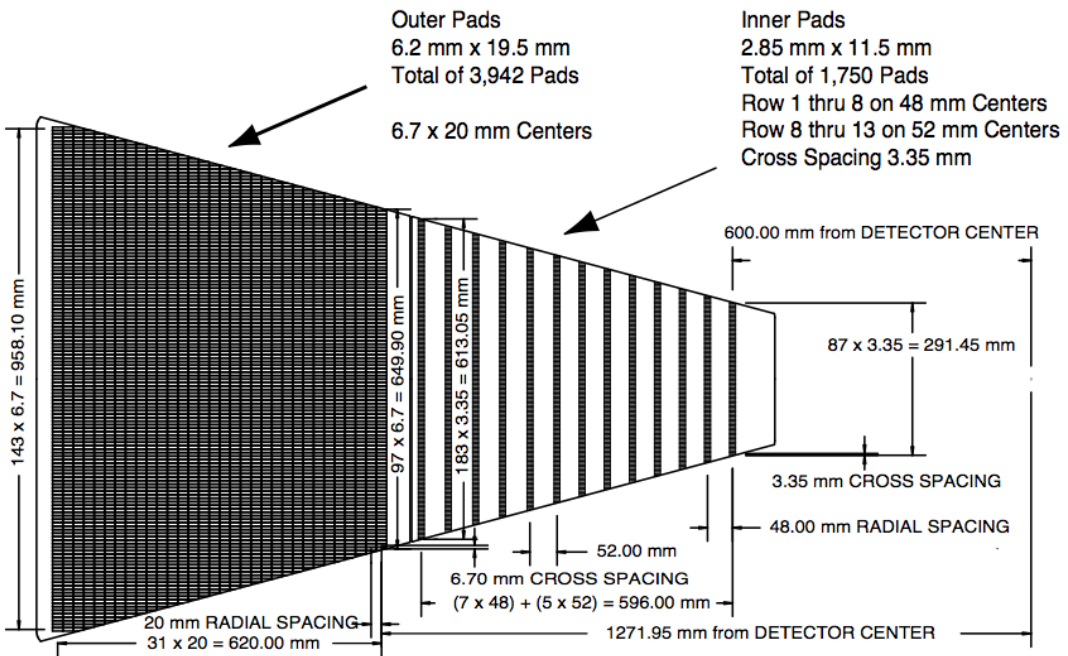


Figure 3.4: One of the 12 anode sectors of the TPC. The outer portion has densely packed pads, while the inner portion is composed of wider rows.

As the drifting electrons reach the anode grid an avalanche occurs triggering a temporary image charge to be induced on the read out pads. The width of each read out pad is chosen such that only three read out pads will share the signal from a single avalanche. This allows for the best centriod reconstruction. The grid of read out pads is broken up into two sections. The outer portion of the grid has continuously packed read-out pads measuring 6.7mm by 20mm optimized for good dE/dx resolution. These pads are located 4mm behind the anode grid. The inner portion has smaller read out pads measuring 3.35 mm by 12 mm optimized for good 2 hit detection. This helps with the large track density seen in the inner portion of the TPC. Unfortunately the available space for electronics for the small pads isn't large enough to have continuous coverage as in the outer section. Instead they are arrange in stripes as seen in figure ???. This arrangement prohibits the inner section to be much help in dE/dx resolution. [4]

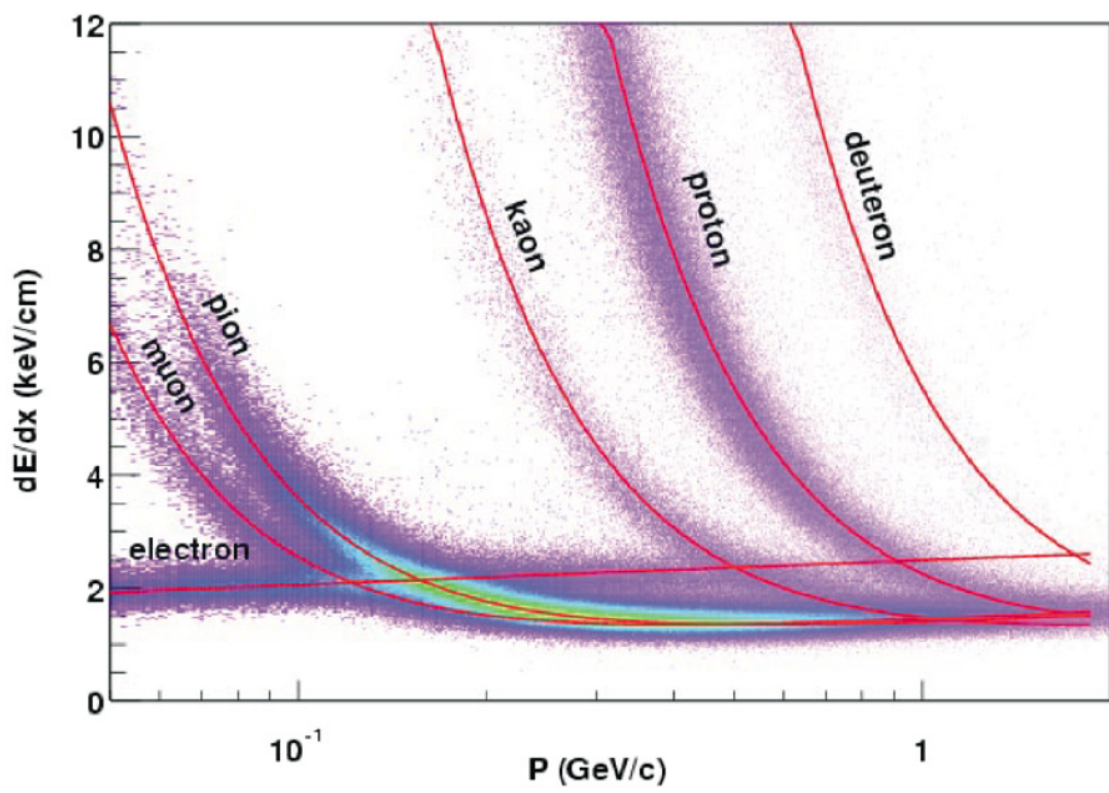


Figure 3.5: Ionization energy loss in TPC gas. Different species show different energy loss signature. This aids in particle identification.

## Barrel Electromagnetic Calorimeter

The Barrel Electromagnetic Calorimeter (BEMC) is a large array of lead and plastic scintillator sitting outside the TPC and inside the STAR magnet. At  $\eta = 0$  the BEMC is roughly 20 radiation lengths thick allowing it to contain electromagnetic showers up to 60 GeV. Scintillation light is carried from the BEMC array to outside the STAR magnet where it is fed into photomultiplier tubes (PMT).

The BEMC is composed of a total of 4800 towers, each one subtending  $0.05^\circ$  in  $\phi$  and 0.05 units in  $\eta$ . A tower consists of 20 layers of 5 mm thick lead, 19 layers of 5mm thick scintillator, and two layers of 6 mm thick scintillator. Each tower is angled toward the reaction region as seen in figure 3.7.

The BEMC is equipped with a pre-shower detector which provide readings of the longitudinal shower development after 1 to 1 and a half radiation lengths. Made up of the first two (6 mm) scintillating layers of the tower, the pre-shower detector aids in distinguishing between  $\pi^0$  and  $\gamma$  as well as between electrons and hadrons. Electrons will typically have a larger ionization energy loss  $dE/dx$  inside the BEMC than hadrons resulting in roughly 63% of electrons showering before the pre-shower volume and 84% by the middle of the pre-shower detector compared to only 3% and 6% for hadrons. The pre-shower detector consists of two 6 mm thick layers of scintillator instead of the 5 mm thick scintillator layers in the rest of the BEMC.

The active scintillating layers, both pre-shower and regular, are made of Kuraray SCSN81 and light from each layer is carried out with wavelength shifting fiber embedding into the scintillator layer. The scintillation light from each layer is transferred to a 2.1 m long optical cable which carries it passed the magnet to a decoder box. Here the light from all 21 layers in a tower, including the two pre-shower layers, are combined and fed into a single PMT. The pre-shower detector also passes a second sample of scintillation light

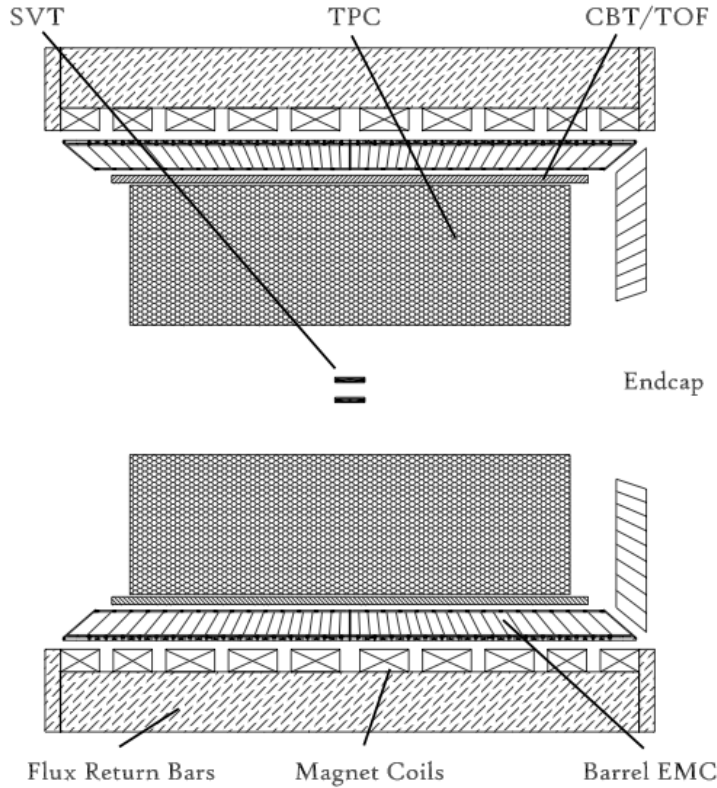


Figure 3.6: The BEMC is located outside the TPC but inside the STAR magnet and return bars. The scintillation light is transported past the magnet and return bars where it is read out by PMTs.

from layers 1 and 2 to a separate PMT, this time not combined with light from any other layers.

As neutral particles, such as  $\pi^0$ , do not ionize the TPC gas, the BEMC is tasked with providing spacial resolution of such species. Instead of making size of each tower of the BEMC comparable to the Moliere radius in the lead, plastic scintillator a shower maximum detector (SMD) is added into the BEMC. The SMD, set at about 5.6 radiation lengths at  $\eta = 0$ , is composed of an aluminum plate with divots on either side. As seen in figure ??, a  $50\mu\text{m}$  gold-plated tungsten anode wire lies in each divot. The wires run along the barrel. As the electromagnetic shower passes these wires a charge is induced. This charge

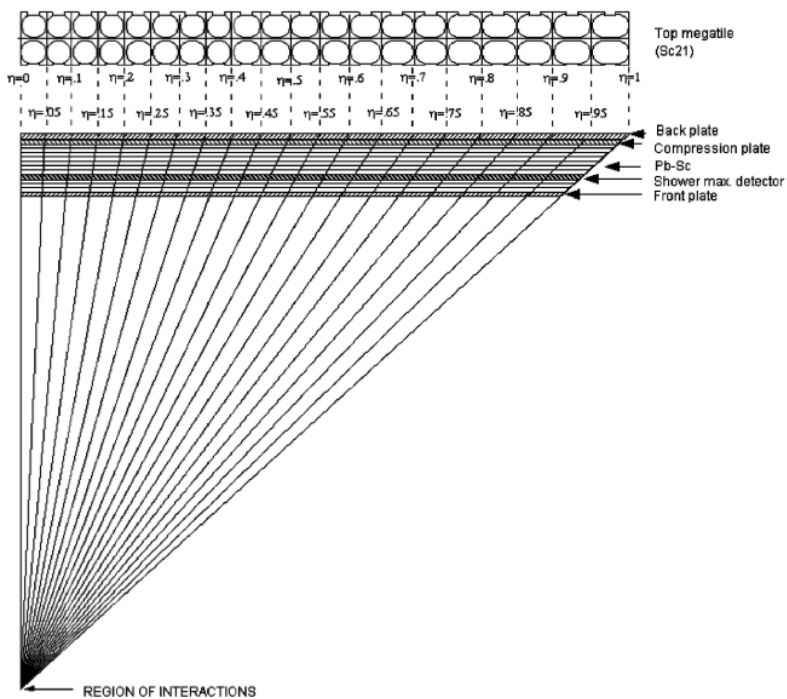


Figure 3.7: Each tower of the BEMC is angled to point back to the interaction region of STAR. The shower max detector as well as the individual scintillator/lead layers are shown.

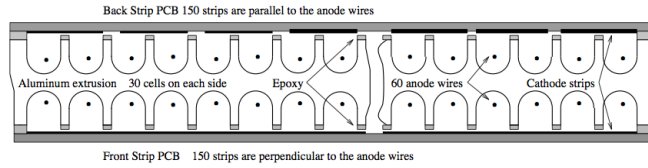


Figure 3.8: Cross sectional view of the shower max detector. Aluminum extrusion in the center containing two sets of anode wires. Cathode strips on the top and bottom face run either parallel or perpendicular to the anode wires.

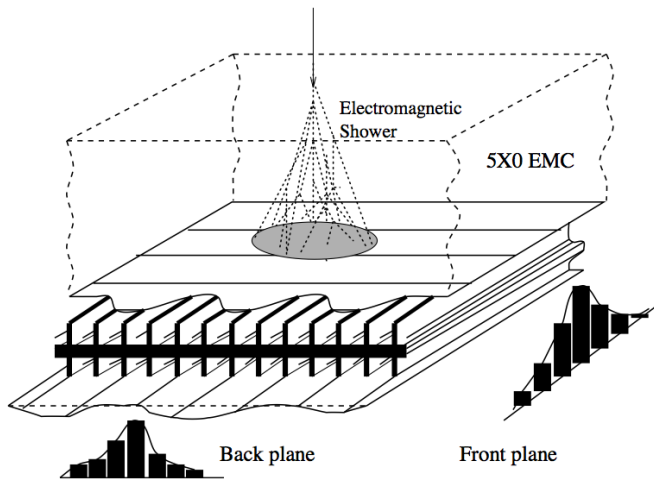


Figure 3.9: Schematic of spatial reconstruction in SMD. The cathode strips on the top and bottom faces read the induced charge in the  $\phi$  and  $\eta$  directions separately.

is amplified by the gas in the divot. Detection strips are located on the top and bottom faces of the aluminum plate. One set of strips runs parallel to the wires and provides the spacial distribution of the shower in the  $\eta$  direction. The other set, running perpendicular to the wires provides the spacial distribution in the  $\phi$  direction. A schematic of this is shown in figure ???. Together They give a full description of the shower position.[6]

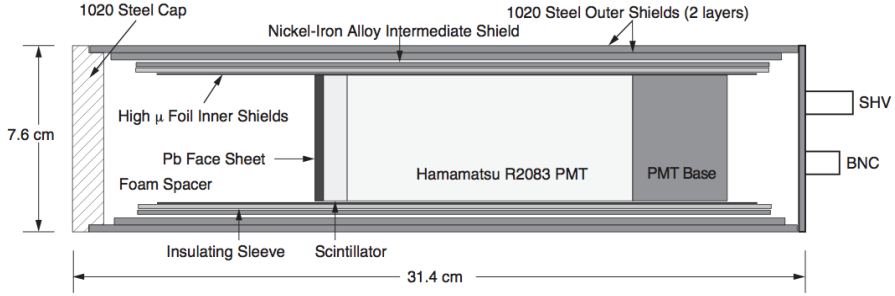


Figure 3.10: A cross section of a pVPD detector element.

## Endcap Electromagnetic Calorimeter

### Time of Flight

To aid in particle identification STAR has a time of flight system. The system is composed of two different detectors, the Time of Flight Patch (TOFp) and the Pseudo Vertex Position Detector (pVPD). Together these detectors allow for direct  $2\sigma \pi/K/p$  identification for track momenta up to about 1.7 GeV/c.

The pVPD is responsible for starting the clock of the time of flight system. It consists of two plastic scintillator detectors, one on either side of the STAR interaction region sitting 5.6 m away from the center of the STAR detector. Both are positioned very close to the beam pipe and detect very forward, high energy photons produced in the collision. The average of the time for both detectors to see this photon pulse is declared the "start time" for the event. The scintillation light is read out by PMTs. The magnetic field strength near the pVPD is on the order of a few hundred Gauss. Because of this the PMTs are shielded on the sides with a steel outer shield, a nickel-Iron alloy intermediate shield, and finally a foil inner shield. They are also shielded from the front with a lead face sheet and a steel cap. A pVPD detector element is shown in figure 3.10. This is mounted to the beam pipe support structure as shown in figure 3.11.

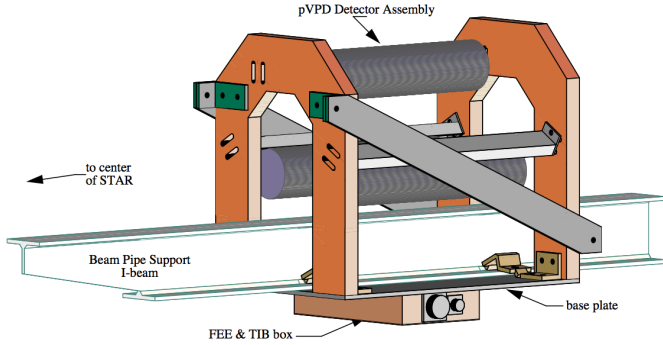


Figure 3.11: The pVVD detector is mounted in the assembly.

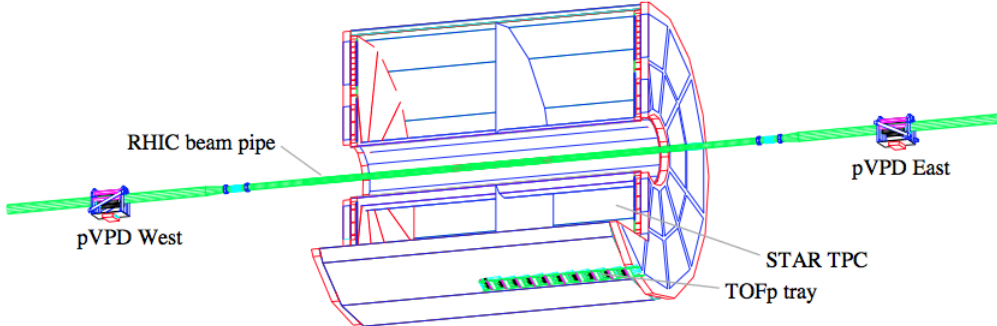


Figure 3.12: The Time of Flight Patch is located near the bottom of the STAR detector at the 7 o'clock position. Also shown here are the two pVVD detectors on either side of the STAR detector.

The pVVD starts the clock for the event and the TPCp stops it. The TPCp, shown in figure 3.12, is again a scintillator/PMT detector. It covers about one unit in  $\eta$  and about 1/60 of STAR's azimuthal coverage. It is encapsulated in an aluminum tray which is fastened to the outer field cage of the TPC at the 7 o'clock position. There are a total of 41 detector assemblies, each consisting of a  $3.81 \times 2 \times 10 \text{ cm}^3$  BC420 plastic scintillator and a PMT. The PMTs are specially designed to work inside the STAR magnet.[11]

Once the clock is stopped a value of  $\beta$  for the track can be calculated as in equation 3.1.

$$\frac{1}{\beta} = \frac{c\tau}{s} \quad (3.1)$$

Here  $c$  is the speed of light,  $\tau$  is the time measured by the time of flight system, and  $s$  is the path length of the track using the reconstructed path of the TPC. From here the mass of the particle can be found using the momentum of the track measured in the TPC.

$$M^2 = \frac{p^2}{\beta^2} - 1 \quad (3.2)$$

### 3.3 STAR triggers

### 3.4 Particle Identification

## 4 Theoretical background

The differential cross section for the scattering process  $P^\dagger P \rightarrow \pi^+ \pi^- + X$

The differential cross section for a transversely polarized quark,  $a$ , in a transversely polarized proton scattering off an unpolarized quark,  $a$ , in an unpolarized proton then fragmenting into a  $\pi^+ \pi^-$  pair is given in equation 4.1.

$$d\sigma_{UT} = 2P_T^{\pi^+\pi^-} \sum_{a,b,c,d} |\vec{s}_a| \sin(\phi_{RS}) \int \frac{dx_a dx_b}{8\pi^2 z_c} h_1(x_a) f_1(x_b) \frac{d\Delta\hat{\sigma}_{a^\dagger b \rightarrow c^\dagger d}}{d\hat{t}} \times \sin\theta H_1^{\triangleleft c} (z_c, \cos\theta, M_{inv}^{\pi^+\pi^- 2}) \quad (4.1)$$

Here  $|\vec{s}_a|$  is the spin direction of the polarized proton. In our experiment we always want the polarized proton's spin to be either up or down. However we can't always tell if it is 100% polarized so we use the polarization of the fill as  $|\vec{s}_a|$ . Moving on,  $\phi_{RS}$  is the relative orientation of the outgoing pion pair shown in figure 4.1,  $z_c$  is the fraction of the fragmenting quark energy the pion pair retains, and  $\theta$  is the azimuthal angle of the outgoing  $\pi^+ \pi^-$  pair.

We can make better sense of the above equation by looking closely at each part. First we see the magnitude of the  $\pi^+ \pi^-$  pair transverse momentum. We then see the polarization of the beam. Next is the sinusoidal modulation of the production of  $\pi^+ \pi^-$  pairs. Inside the integral we have the transversity distribution function  $h_1$  due to the transversely

polarized quark  $a$  and the unpolarized fragmentation function  $f_1$  due to the unpolarized quark  $b$ . After this we see the elementary scattering cross section of an unpolarized quark  $a$  scattering off a transversely polarized quark  $a$  into a transversely polarized quark  $c$  and an unpolarized quark  $d$ . Quark  $c$  goes on to fragment into  $\pi^+\pi^- + X$  described by the IFF  $H_1^\triangleleft$  while  $d$  goes undetected.

Comparing this to the cross section when both initial state quarks are unpolarized we see several similarities.

$$d\sigma_{UU} = 2P_T^{\pi^+\pi^-} \sum_{a,b,c,d} \int \frac{dx_a dx_b}{8\pi^2 z_c} f_1^a(x_a) f_1^b(x_b) \frac{d\hat{\sigma}_{ab \rightarrow cd}}{dt} D_1^c(\bar{z}_c, \cos\theta_C, M_C^2) \quad (4.2)$$

As similar as equations 4.1 and 4.2 looks there are some important differences worth noting. Obviously the polarization isn't there since we now are dealing with unpolarized scattering. The sinusoidal modulation has also disappeared. The transversity distribution has turned into a second unpolarized distribution, and the IFF has turned into  $D_1^c$  which is the unpolarized counterpart to the IFF.

The most important thing to mention is that the sine modulation seen in unpolarized-polarized (U-T) scattering is not seen in unpolarized-unpolarized (U-U) scattering. This means that there is a bias to the yield of  $\pi^+\pi^-$  pairs in U-T scattering when compared to U-U scattering. We can observe this by looking at the number of  $\pi^+\pi^-$  pairs at a given value of  $\phi_{RS}$  when the polarization of the proton beam is  $\hat{y}$  vs the number when the polarization is  $-\hat{y}$ . We then normalize by the number we see at that value of  $\phi_{RS}$  for U-U scattering.

$$A_{UT} \sin(\phi_{RS}) = \frac{1}{|\vec{s}_a|} \frac{d\sigma^\uparrow - d\sigma^\downarrow}{d\sigma_{UU}} \quad (4.3)$$

In our experiment we never scatter unpolarized protons, so we have to be clever about the cross section seen in the denominator of equation 4.4. If we sum over the two spin

states we are left with the entire unpolarized cross section  $d\sigma^\uparrow + d\sigma^\downarrow = d\sigma_{UU}$ . [cite thesis and papers by becheta also maybe add the jeffe paper and info]

$$A_{UT} \sin(\phi_{RS}) = \frac{1}{|\vec{s}_a|} \frac{d\sigma^\uparrow - d\sigma^\downarrow}{d\sigma^\uparrow + d\sigma^\downarrow} \quad (4.4)$$

Important physics can be seen by preforming a partial wave expansion of the cross section. Namely  $\sin \theta H_1^{\triangleleft}$  can be expanded. Looking at the first two terms in the expansion,

$$\begin{aligned} \sin \theta H_1^{\triangleleft c}(\bar{z}_c, \cos \theta, M_{inv}^{\pi^+ \pi^- 2}) &\approx H_{1,ot}^{\triangleleft c}(\bar{z}_c, M_{inv}^{\pi^+ \pi^- 2}) \sin \theta \\ &+ H_{1,lt}^{\triangleleft c}(\bar{z}_c, M_{inv}^{\pi^+ \pi^- 2}) \sin \theta \cos \theta \end{aligned} \quad (4.5)$$

The first term, S/P wave interference, is due to the interference between amplitudes for a decay into an  $L = 0$   $\pi^+ \pi^-$  pair and an  $L = 1$  transversely polarized  $\pi^+ \pi^-$  pair. The second term, P/P wave interference, is due to the interference between amplitudes for a decay into an  $L = 1$   $\pi^+ \pi^-$  pair and an  $L = 1$  transversely polarized  $\pi^+ \pi^-$  pair. The  $L = 1$  contributions come from a  $\pi^+ \pi^-$  pair that went through a spin-1 intermediate state. One such intermediary we have the ability and statistics to look for is the  $\rho$  meson. We expect there to be an enhancement in the IFF, and thus the asymmetry, in the invariant mass region of the  $\rho$  (770 MeV). [3, 14]

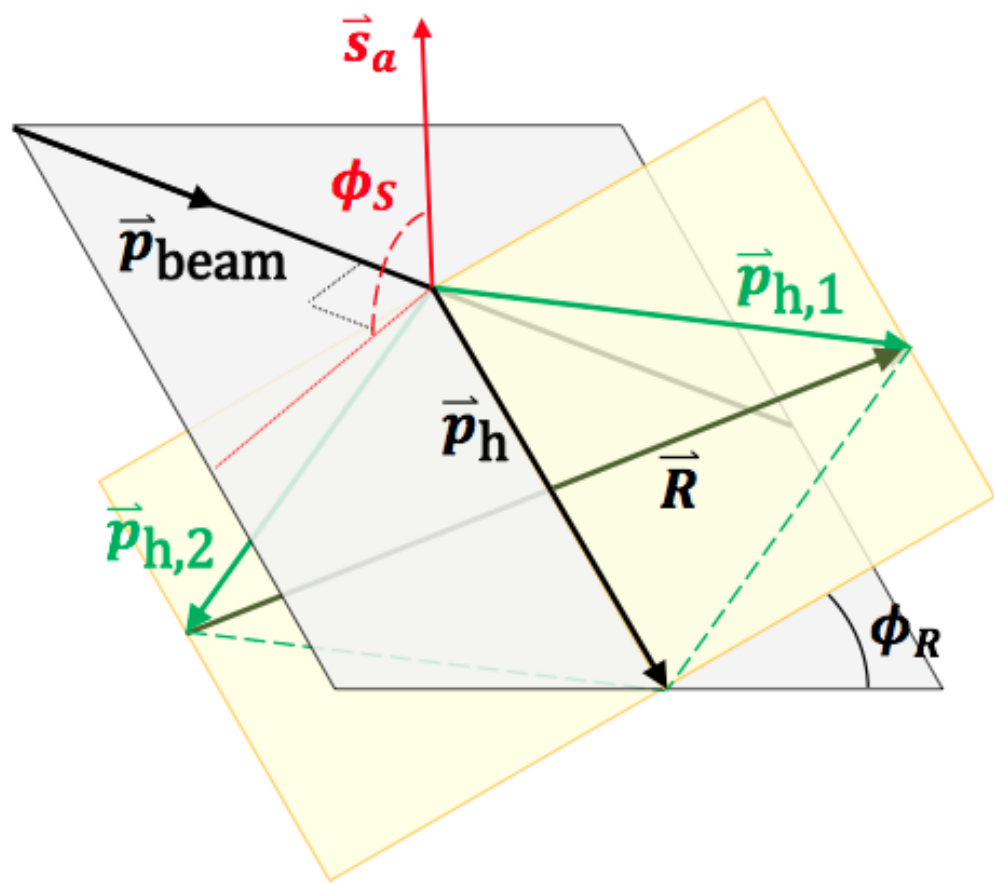


Figure 4.1: Visual representation of angles  $\phi_R$  and  $\phi_s$

## **5 2006 analysis and sim**

The 2006 data set gave us the first glimpse of this asymmetry. The analysis of the 2006 data set was done by Anselm Vossen. The 2006 run had only a small integrated luminosity of 200 GeV transverse proton proton collisions. Due to this, the data set was small and you couldn't look at everything you wanted to.

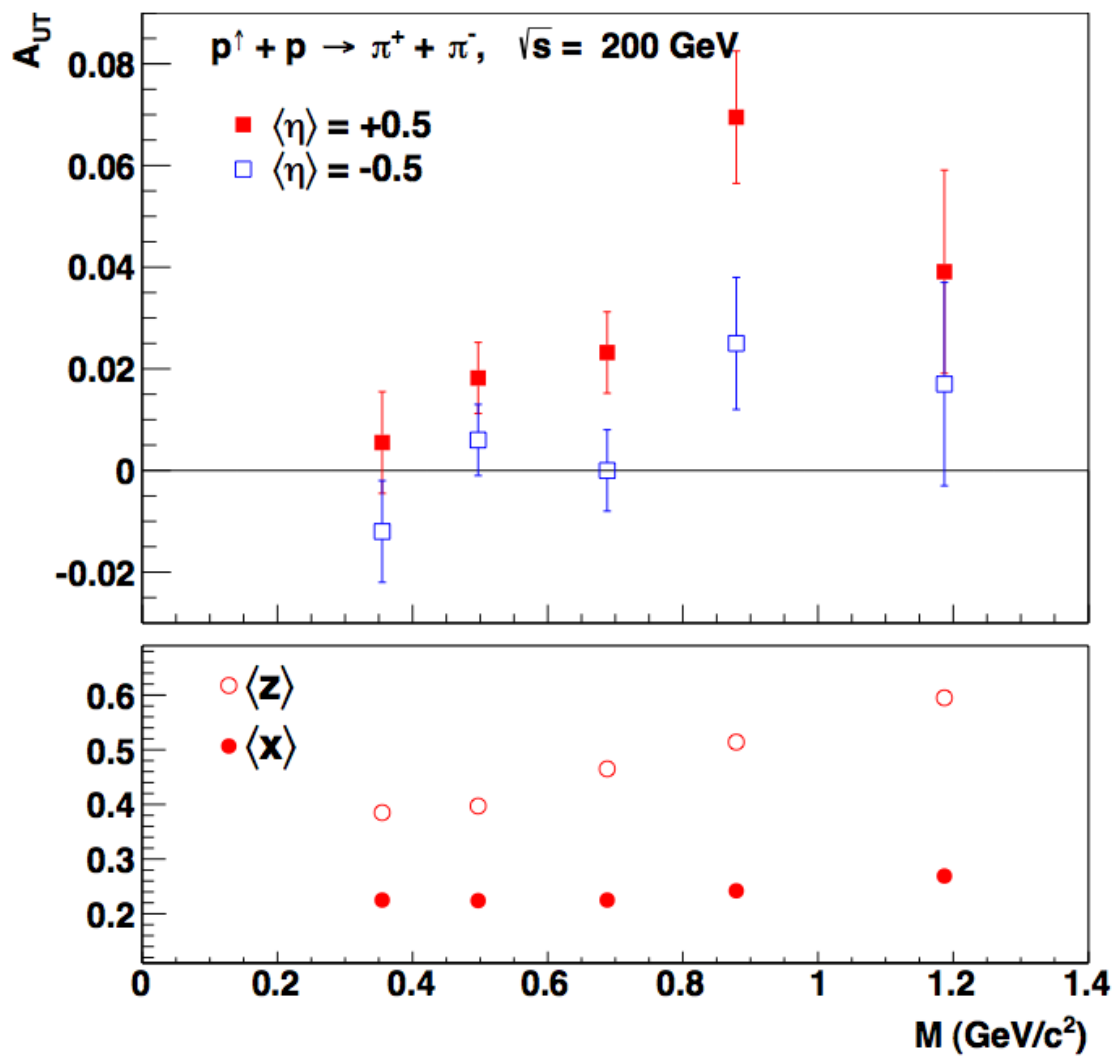


Figure 5.1: Asymmetry versus invariant mass of the  $\pi^+\pi^-$  pair for the 2006 data set

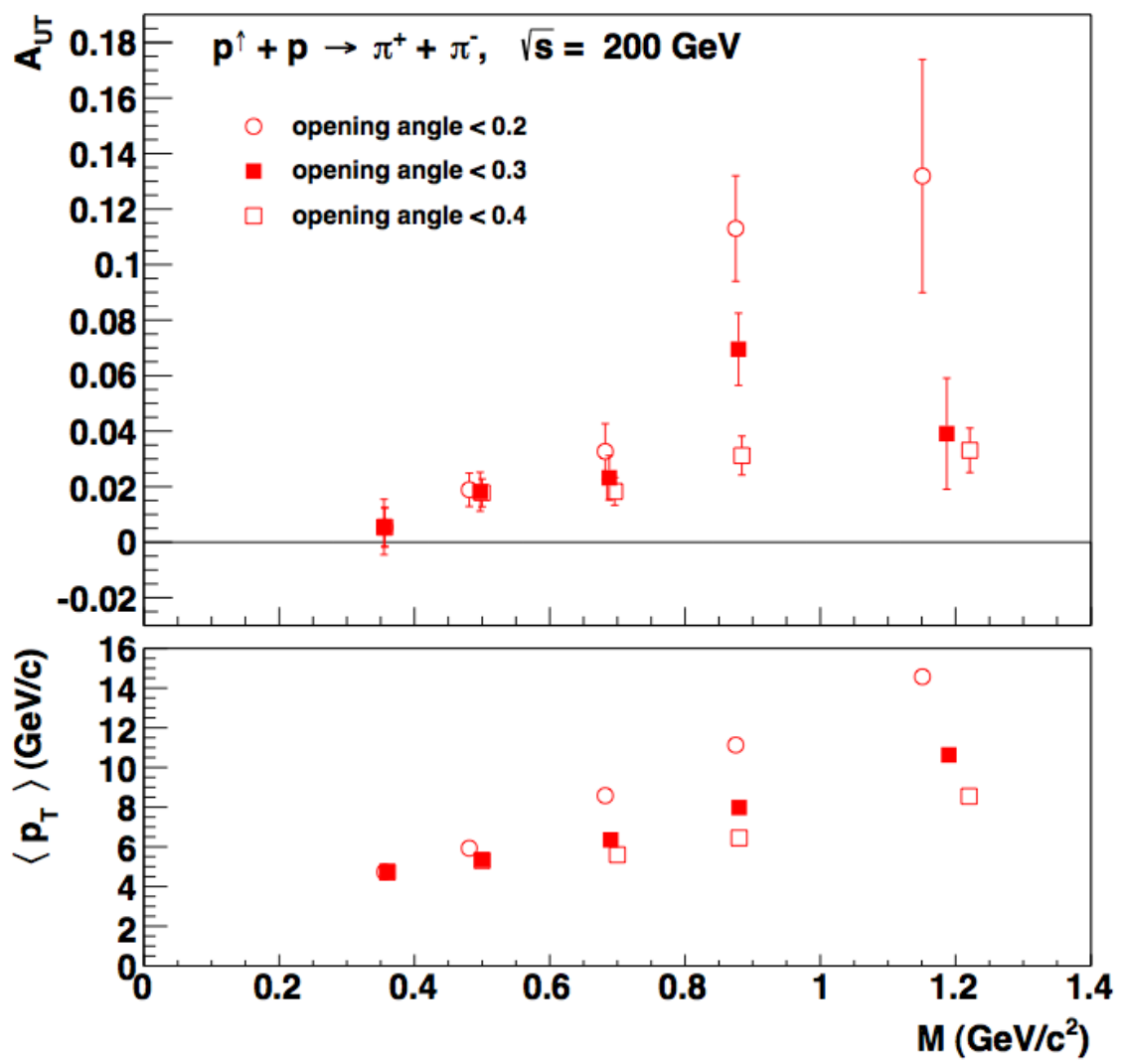


Figure 5.2: Asymmetry versus invariant mass of the  $\pi^+\pi^-$  pair for the 2006 data set

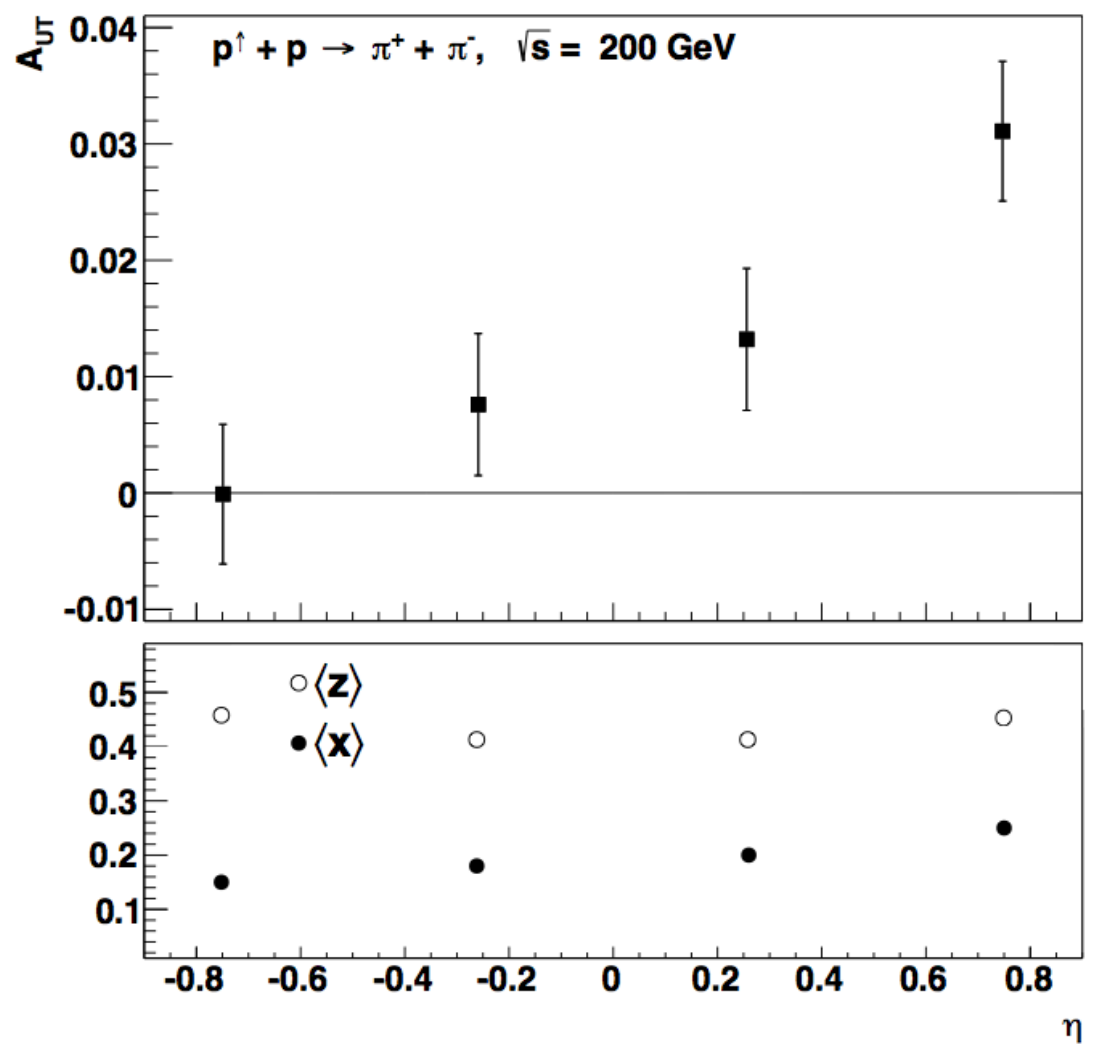


Figure 5.3: Asymmetry versus  $\eta^{\pi^+\pi^-}$  for the 2006 data set

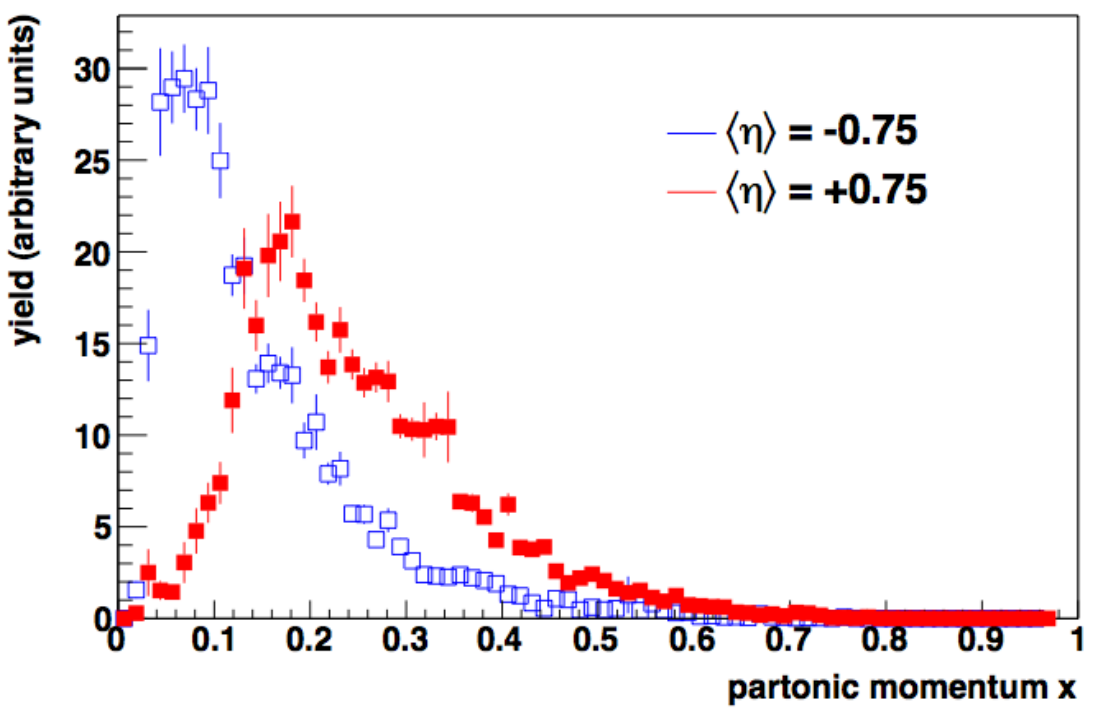


Figure 5.4: Partonic momentum fraction  $x$  for the parton from the polarized proton in the forward (red) and backward (blue) direction

# 6 2012 IFF

## 6.1 Data Set and Cuts?

## 6.2 particle Identification

## 6.3 Finding $\pi^+\pi^-$ Pairs

The first step in finding pion pairs is to select events which are worth looking at. We do this by only concentrating on events which trigger at least one of the following STAR triggers: JP0, JP1, JP2, AJP, BHT0VPD, BHT1VPD, BHT2BBC, or BHT2. Selecting our data based on these triggers introduces a bias to our sample. The effect of this biasing will be discussed in detail in chapter ADD CHAPTER NUMBER FOR 2012 SIMULATION ANALYSIS.

For every event pions are identified by ionization energy loss in the TPC. A value,  $n_\sigma(\pi)$ , is given to each track in an event describing how many standard deviations away it is from an ideal pion on the ionization energy loss curve shown in figure 6.2. If there were only pions, the distribution of  $n_\sigma(\pi)$  values would be normal centered around 0. However as you can see in figure 6.3, the red curve is not a gaussian. This is due to contamination from kaons/protons and electrons. To account for this we fit the  $n_\sigma(\pi)$  distribution with three gaussians. The purple curve centered around zero is what we consider pions, the

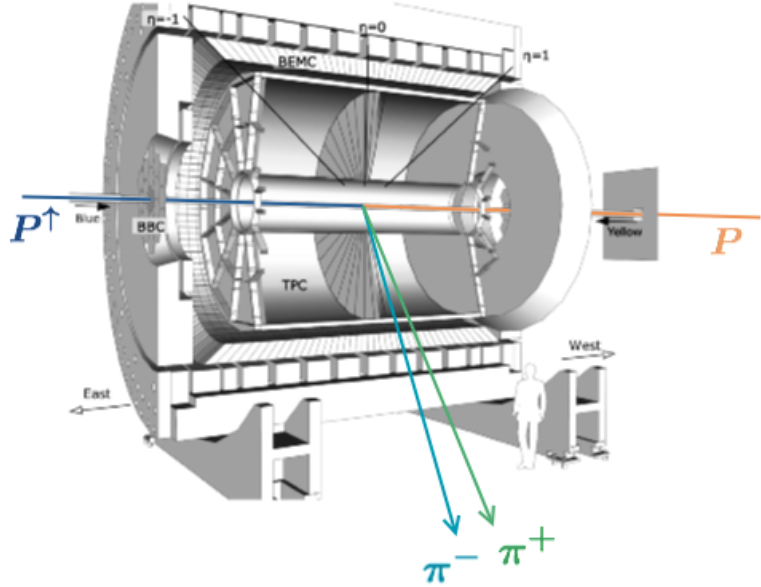


Figure 6.1

green curve centered at -2 are kaons and protons, and the small blue curve at about 3 is electrons. A clean sample of pions can be found by selecting tracks with an  $n_\sigma(\pi)$  between -1 and 2.5. This is shown by the vertical orange lines in figure 6.3. This choice of an  $n_\sigma(\pi)$  range avoids the kaon-proton peak while still allowing the majority of pions. Figure 6.4 shows the contamination from kaons, protons, and electrons for different  $\eta^{\pi^+\pi^-}$ .

Once a clean sample is found  $\pi^+$ s and  $\pi^-$ s must be combined into  $\pi^+\pi^-$  pairs. Every combination of  $\pi^+$  and  $\pi^-$  in an event are checked. They become a pair if they pass the individual track cuts and if they are contained in a cone of a certain radius in  $\eta - \phi$  space (figure). For 1D binning, radii of 0.2, 0.3, and 0.4 are used while 0.7 is used in 2D binning in order to increase statistics.

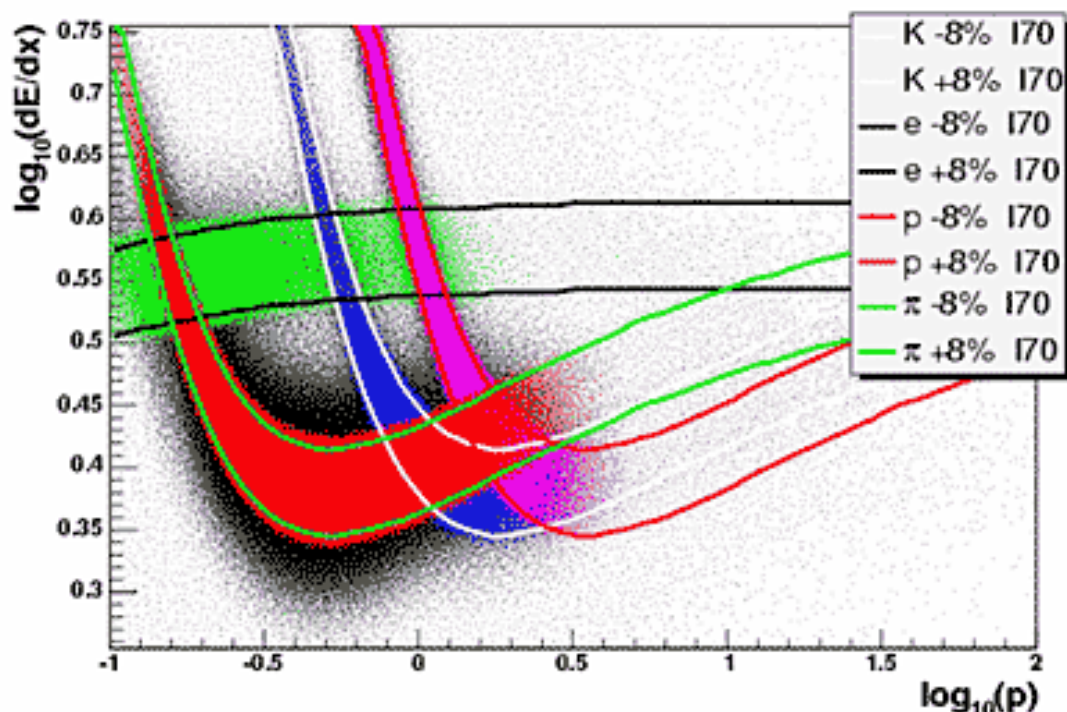


Figure 6.2: ionization energy loss vs momentum in TPC. Tracks in the red band are pions we want to find. The blue and pink band are koans and protons we want minimize in our sample

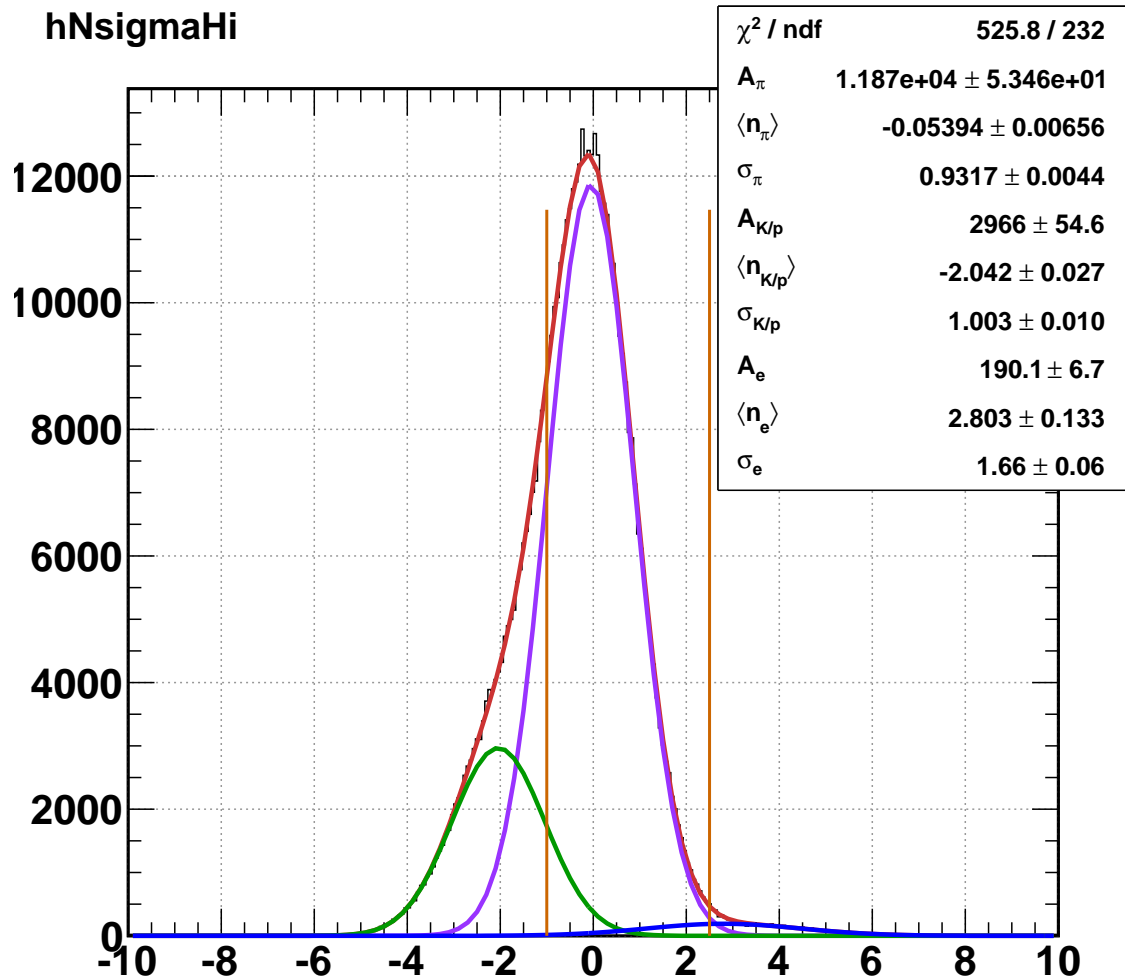


Figure 6.3: Distribution of  $n_\sigma(\pi)$  fit with three Gaussians.

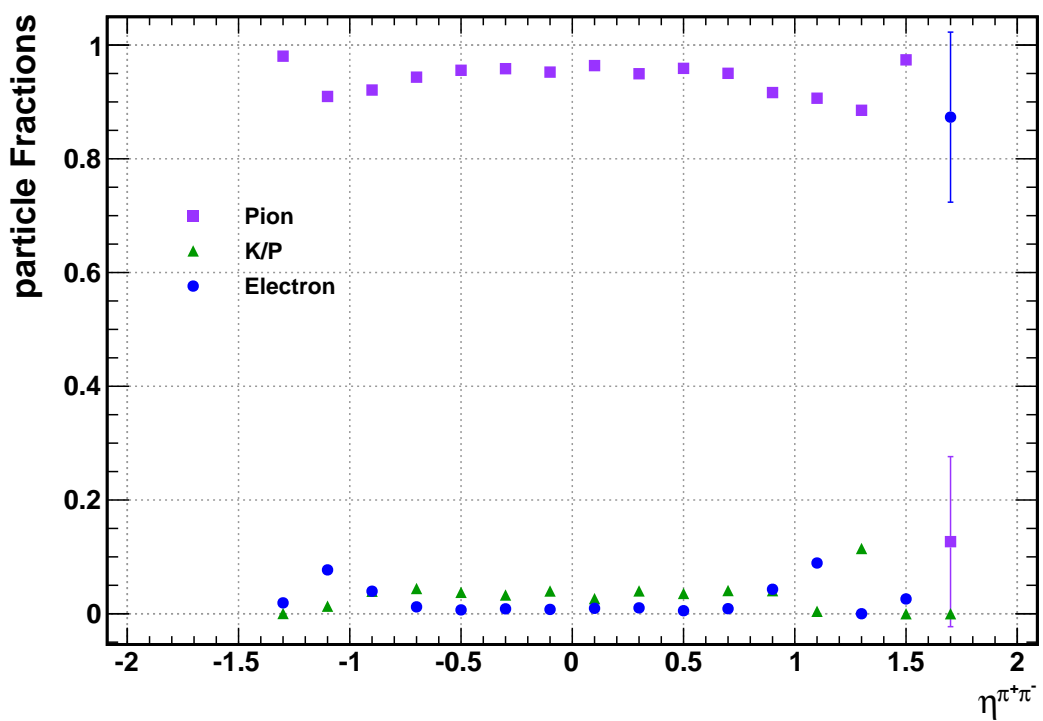


Figure 6.4: contamination from kaon, proton, and electron

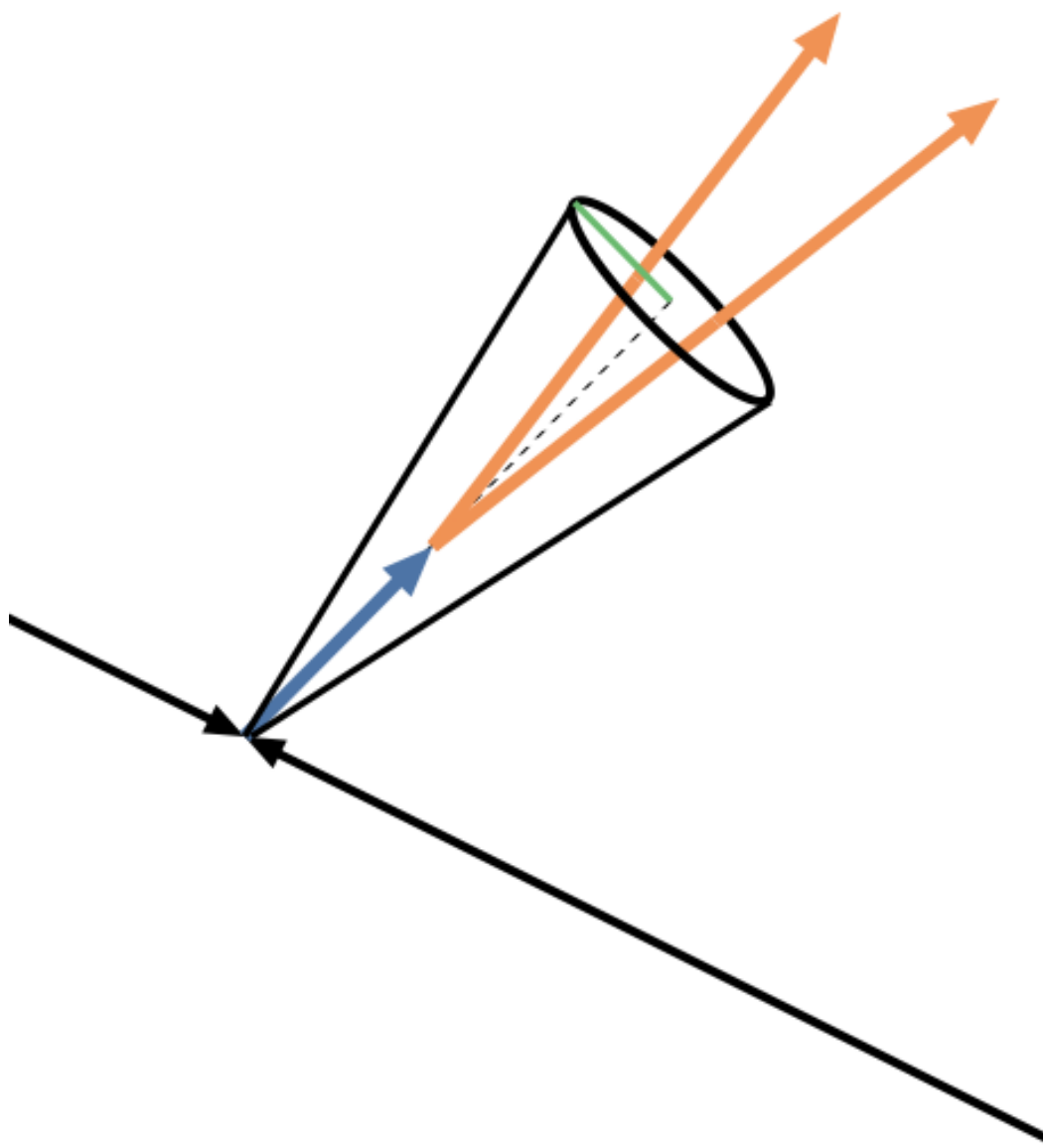


Figure 6.5: radius cut

## 6.4 Pair Distributions

The entire data set provides 11705462  $\pi^+\pi^-$  in a radius larger than 0.05 and 1.0 before trigger information is used. The minimum radius cut of 0.05 is used because when the tracks are very close together, the uncertainty in track position can cause the orientation of the pairs to flip.

Once the data set was ready, quality tests were preformed on the pion pairs. These included looking at the invariant mass, transverse momentum, and pseudorapidity distributions for the pairs.

## 6.5 Determining the angles

### 6.6 Calculating The Asymmetry

#### Luminosity Method

To calculate the asymmetry using the luminosity method,

$$A_{UT}P \sin(\phi_{RS}) = \frac{\frac{N^\uparrow}{L^\uparrow} - \frac{N^\downarrow}{L^\downarrow}}{\frac{N^\uparrow}{L^\uparrow} + \frac{N^\downarrow}{L^\downarrow}} \quad (6.1)$$

$\phi_{RS}$  can take values from  $-\pi$  to  $\pi$

#### Cross Ratio Method

A more clever way of constructing the asymmetry is with the cross ratio method. I break the angle  $\phi_{RS}$  up into 32 bins. I then count the number of pion pairs in that  $\phi_{RS}$  bin when the polarization is up  $N_{\phi_{RS}}^\uparrow$ .

$$N_{\phi_{RS}}^\uparrow = L^\uparrow I_{\phi_{RS}}(\theta) [1 + A_{UT}P \sin(\phi_{RS})] \quad (6.2)$$

In the above equation  $I_{\phi_{RS}}(\theta)$  is the unpolarized cross section into the designated  $\phi_{RS}$  bin and polar angle  $\theta$ . The asymmetry causes an enhancement in the number of pion pairs we see. Next we look at the number of pairs we see in the same  $\phi_{RS}$  bin when the spin is down.

$$N_{\phi_{RS}}^{\downarrow} = L^{\downarrow} I_{\phi_{RS}}(\theta) [1 - A_{UT} P \sin(\phi_{RS})] \quad (6.3)$$

This time the spin is down so the plus sign in equation 6.2 becomes a negative. This tells us that the number of pairs we see from a spin down polarization is decreased. Next we want to look at what happens when we change the  $\phi_{RS}$  bin by  $\pi$ . Still counting when the polarization is spin down we see that:

$$N_{\phi_{RS}+\pi}^{\downarrow} = L^{\downarrow} I_{\phi_{RS}+\pi}(\theta) [1 + A_{UT} P \sin(\phi_{RS})] \quad (6.4)$$

Since  $\sin(x + \pi) = -\sin(x)$ , the negative sign from equation 6.3 has flipped again. Finally if we look at bin  $\phi_{RS} + \pi$ , with a spin up polarization we see the sign flip one more time.

$$N_{\phi_{RS}+\pi}^{\uparrow} = L^{\uparrow} I_{\phi_{RS}+\pi}(\theta) [1 - A_{UT} P \sin(\phi_{RS})] \quad (6.5)$$

We then define "left" and "right"<sup>1</sup> as

$$\mathcal{L} = \sqrt{N_{\phi_{RS}}^{\uparrow} N_{\phi_{RS}+\pi}^{\downarrow}} = \sqrt{L^{\uparrow} L^{\downarrow} I_{\phi_{RS}} I_{\phi_{RS}+\pi}} [1 + A_{UT} P \sin(\phi_{RS})] \quad (6.6)$$

$$\mathcal{R} = \sqrt{N_{\phi_{RS}}^{\downarrow} N_{\phi_{RS}+\pi}^{\uparrow}} = \sqrt{L^{\uparrow} L^{\downarrow} I_{\phi_{RS}} I_{\phi_{RS}+\pi}} [1 - A_{UT} P \sin(\phi_{RS})] \quad (6.7)$$

The combination  $\frac{\mathcal{L}-\mathcal{R}}{\mathcal{L}+\mathcal{R}}$  gives an expression independent of luminosities.

---

<sup>1</sup>Called left and right because the cross ratio was first used in experiments measuring asymmetries in particle production detected in two different detectors. One of these detectors was situated to the left of the incident beam and the other to the right.

$$\frac{\mathcal{L} - \mathcal{R}}{\mathcal{L} + \mathcal{R}} = \frac{\sqrt{N_{\phi_{RS}}^{\uparrow} N_{\phi_{RS}+\pi}^{\downarrow}} - \sqrt{N_{\phi_{RS}}^{\downarrow} N_{\phi_{RS}+\pi}^{\uparrow}}}{\sqrt{N_{\phi_{RS}}^{\uparrow} N_{\phi_{RS}+\pi}^{\downarrow}} + \sqrt{N_{\phi_{RS}}^{\downarrow} N_{\phi_{RS}+\pi}^{\uparrow}}} = A_{UT} P \sin(\phi_{RS}) \quad (6.8)$$

This Equation (6.8) is called the cross ratio method and what I will use throughout my analysis. As stated, this form of the asymmetry is nice because luminosity and detector effects are canceled. This helps us for multiple reasons. The uncertainty in luminosity is difficult to pin down as the luminosity can fluctuate. So not having to take this into account is good. Also detector irregularities causing more pairs to be found near a "hot tower" are canceled. One thing to note is that only 16 of my original 32  $\phi_{RS}$  bins are unique because I have double counted. This is because I use the same number for  $N_{\phi_{RS}}^{\uparrow}$  for  $\phi_{RS}$  bin 1 and for  $N_{\phi_{RS}+\pi}^{\uparrow}$  for  $\phi_{RS}$  bin 9. The unique range of  $\phi_{RS}$  I choose to use is  $-\pi/2$  to  $\pi/2$

In order to extract the asymmetry, a histogram of  $\frac{1}{P} \frac{\mathcal{L} - \mathcal{R}}{\mathcal{L} + \mathcal{R}}$  is constructed. This is then fit with a sine function ( $A \sin(\phi_{RS})$ ), and the resulting amplitude of the fit is taken as  $A_{UT}$ . This is done for different kinematic bins. An example of this fitting is shown in figure 6.7.

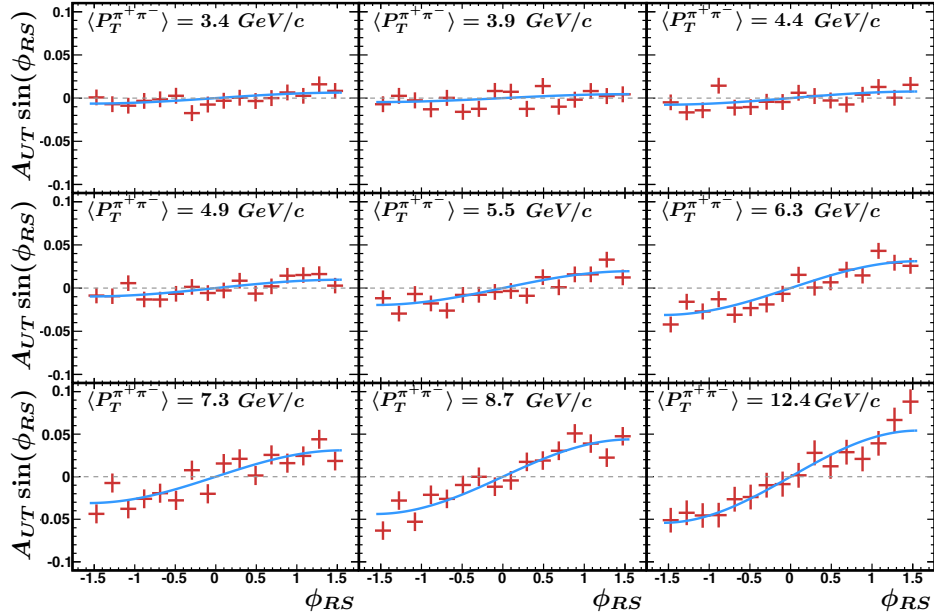


Figure 6.6: Example of the sine fitting. Here different pair transverse momentum ranges are fit with a sine. as the transverse momentum increases, the amplitude of the fit, and thus the asymmetry  $A_{UT}$ , increases.

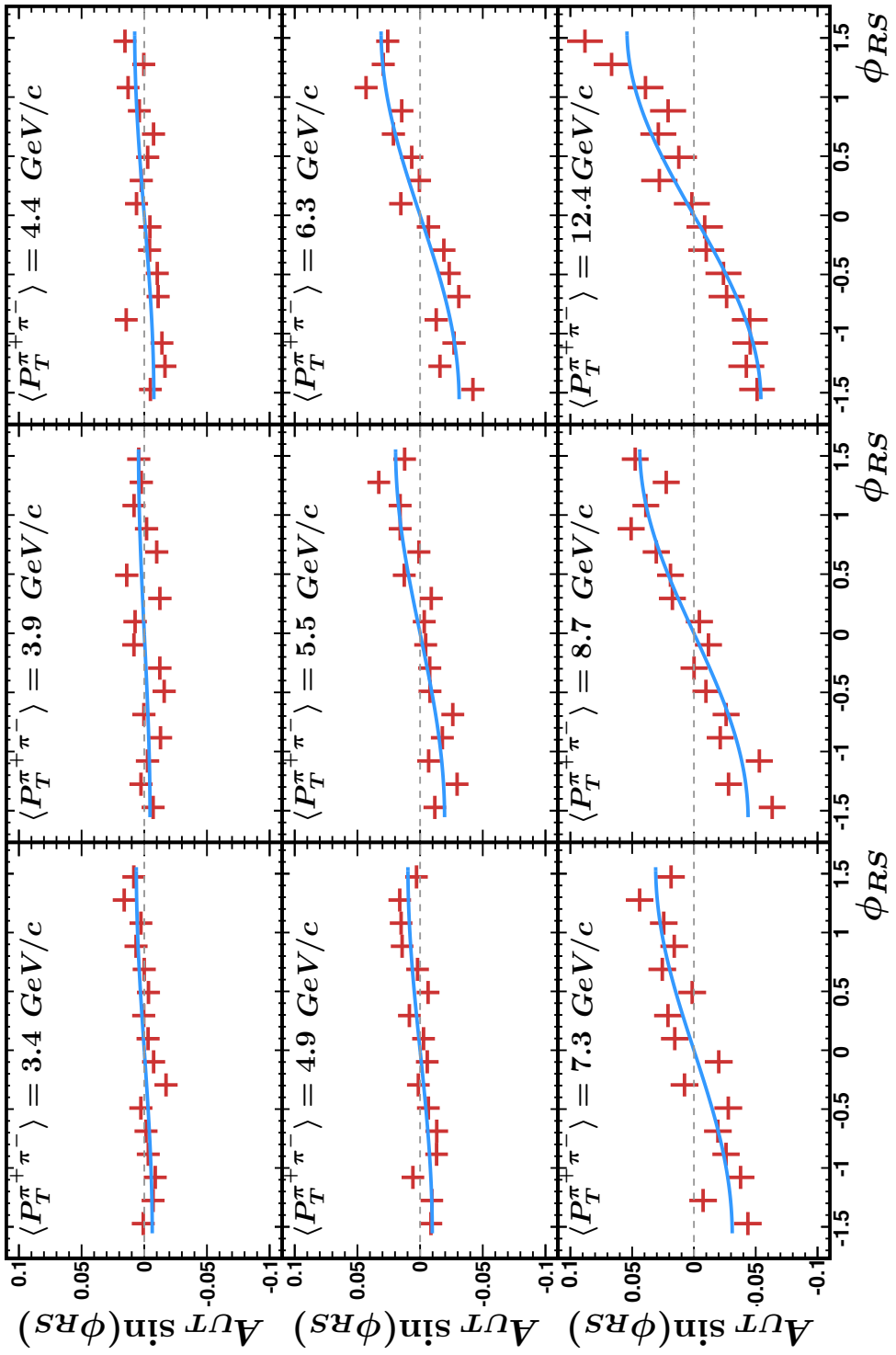


Figure 6.7: Example of the sine fitting. Here different pair transverse momentum ranges are fit with a sine. as the transverse momentum increases, the amplitude of the fit, and thus the asymmetry  $A_{UT}$ , increases.

# 7 Results

## 7.1 One Dimensional Kinematic Binning

## 7.2 Check For False Asymmetries

In order to make sure the asymmetries we detect are not caused by some detector factor or an error in the code, we perform checks on situations we think will show zero asymmetry. The first check is done by analyzing the same data but randomly assigning a spin state to the polarized proton. A randomly assigned spin is assigned correctly half the time and incorrectly the other half. Looking at the cross ratio formula from earlier (eq 6.8) for both cases we see the asymmetry should vanish. The correct spin assignment is represented to the left of the plus sign in equation 7.1, and the incorrect assignment to the right. The incorrect assignment is taken into account by the change in the spin orientation superscripts right of the plus sign in equation 7.1. The two factors cancel exactly with enough statistics and should lead to zero observed asymmetry.

$$\frac{1}{2} \frac{\sqrt{N_{\phi_{RS}}^{\uparrow} N_{\phi_{RS}+\pi}^{\downarrow}} - \sqrt{N_{\phi_{RS}}^{\downarrow} N_{\phi_{RS}+\pi}^{\uparrow}}}{\sqrt{N_{\phi_{RS}}^{\uparrow} N_{\phi_{RS}+\pi}^{\downarrow}} + \sqrt{N_{\phi_{RS}}^{\downarrow} N_{\phi_{RS}+\pi}^{\uparrow}}} + \frac{1}{2} \frac{\sqrt{N_{\phi_{RS}}^{\downarrow} N_{\phi_{RS}+\pi}^{\uparrow}} - \sqrt{N_{\phi_{RS}}^{\uparrow} N_{\phi_{RS}+\pi}^{\downarrow}}}{\sqrt{N_{\phi_{RS}}^{\downarrow} N_{\phi_{RS}+\pi}^{\uparrow}} + \sqrt{N_{\phi_{RS}}^{\uparrow} N_{\phi_{RS}+\pi}^{\downarrow}}} = 0 \quad (7.1)$$

You can see in figure 7.2 we see no false asymmetry for random proton spin assignment.

Just as we randomly assigned the spin state of the proton, we also randomly assign the charges on the  $\pi^+, \pi^-$ . This changes the direction of  $\vec{R}$ .

$$\sin(\phi_R) = \frac{(P_B \times R) \hat{P}_h}{|\hat{P}_h \times P_B| |\hat{P}_h \times R|} \quad (7.2)$$

$$\cos(\phi_R) = \frac{\hat{P}_h \times P_B}{|\hat{P}_h \times P_B|} \frac{\hat{P}_h \times R}{|\hat{P}_h \times R|} \quad (7.3)$$

By making the substitution  $R \rightarrow -R$  in equations 7.2 and 7.3, it is seen that  $\phi_R \rightarrow \phi_R + \pi$  (or  $\phi_R \rightarrow \phi_R - \pi$  because I keep  $\phi_R$  in the range  $-\pi$  to  $\pi$ ). Since  $R$  doesn't appear in the definition of  $\sin(\phi_S)$  or  $\cos(\phi_S)$ ,  $\phi_S$  is unchanged. This leads to  $\phi_{RS} \rightarrow \phi_{RS} + \pi$  (or  $\phi_{RS} \rightarrow \phi_{RS} - \pi$  because I constrain the angle to be in the range  $-\pi$  to  $\pi$ ). Just like the random spin assignment, the random pion charge assignment will be correct half the time and incorrect the other half. By looking at the cross ratio for each case we come to an equation similar to equation 7.1 with both factors canceling.

$$\frac{1}{2} \frac{\sqrt{N_{\phi_{RS}}^\uparrow N_{\phi_{RS}+\pi}^\downarrow} - \sqrt{N_{\phi_{RS}}^\downarrow N_{\phi_{RS}+\pi}^\uparrow}}{\sqrt{N_{\phi_{RS}}^\uparrow N_{\phi_{RS}+\pi}^\downarrow} + \sqrt{N_{\phi_{RS}}^\downarrow N_{\phi_{RS}+\pi}^\uparrow}} + \frac{1}{2} \frac{\sqrt{N_{\phi_{RS}+\pi}^\uparrow N_{\phi_{RS}}^\downarrow} - \sqrt{N_{\phi_{RS}+\pi}^\downarrow N_{\phi_{RS}}^\uparrow}}{\sqrt{N_{\phi_{RS}+\pi}^\uparrow N_{\phi_{RS}}^\downarrow} + \sqrt{N_{\phi_{RS}+\pi}^\downarrow N_{\phi_{RS}}^\uparrow}} = 0 \quad (7.4)$$

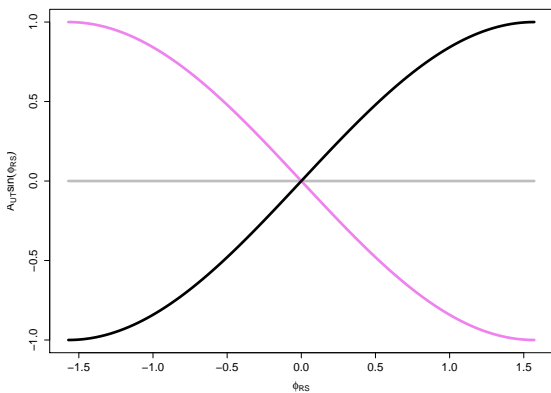


Figure 7.1: When the spin is randomly assigned correctly the relationship between  $\frac{1}{P} \frac{\mathcal{L} - \mathcal{R}}{\mathcal{L} + \mathcal{R}}$  and  $\phi_{RS}$  is a sine (black). When it is randomly assigned incorrectly the relationship is reversed (violet). Since it is assigned correctly on average half the time and incorrectly half the time, the result is zero (grey).

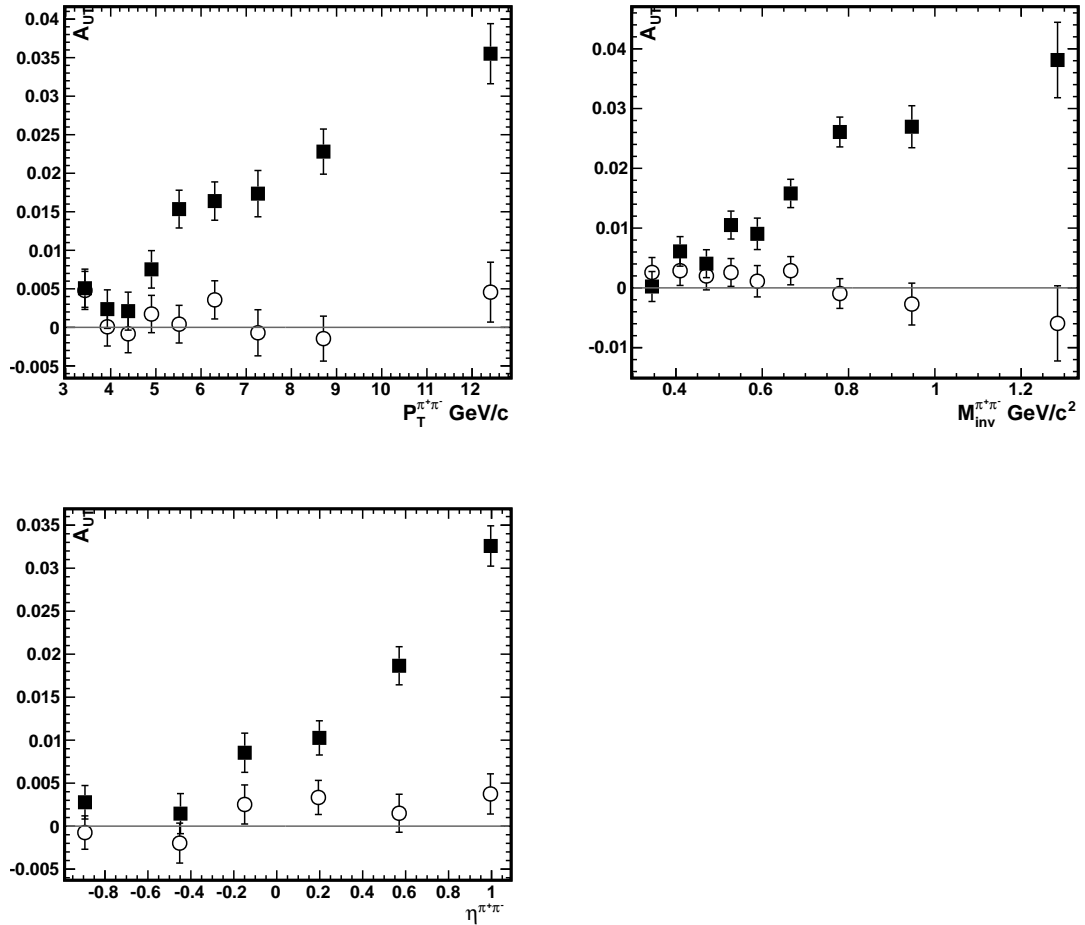


Figure 7.2: Randomly assigned pion charges (open circles) show no sign of asymmetry in any kinematic variable. Correct assignment (solid squares) shown for comparison.  $-2 < \eta^{\pi^+\pi^-} < 2$  for  $P_T^{\pi^+\pi^-}$  and  $M_{inv}^{\pi^+\pi^-}$  plots.

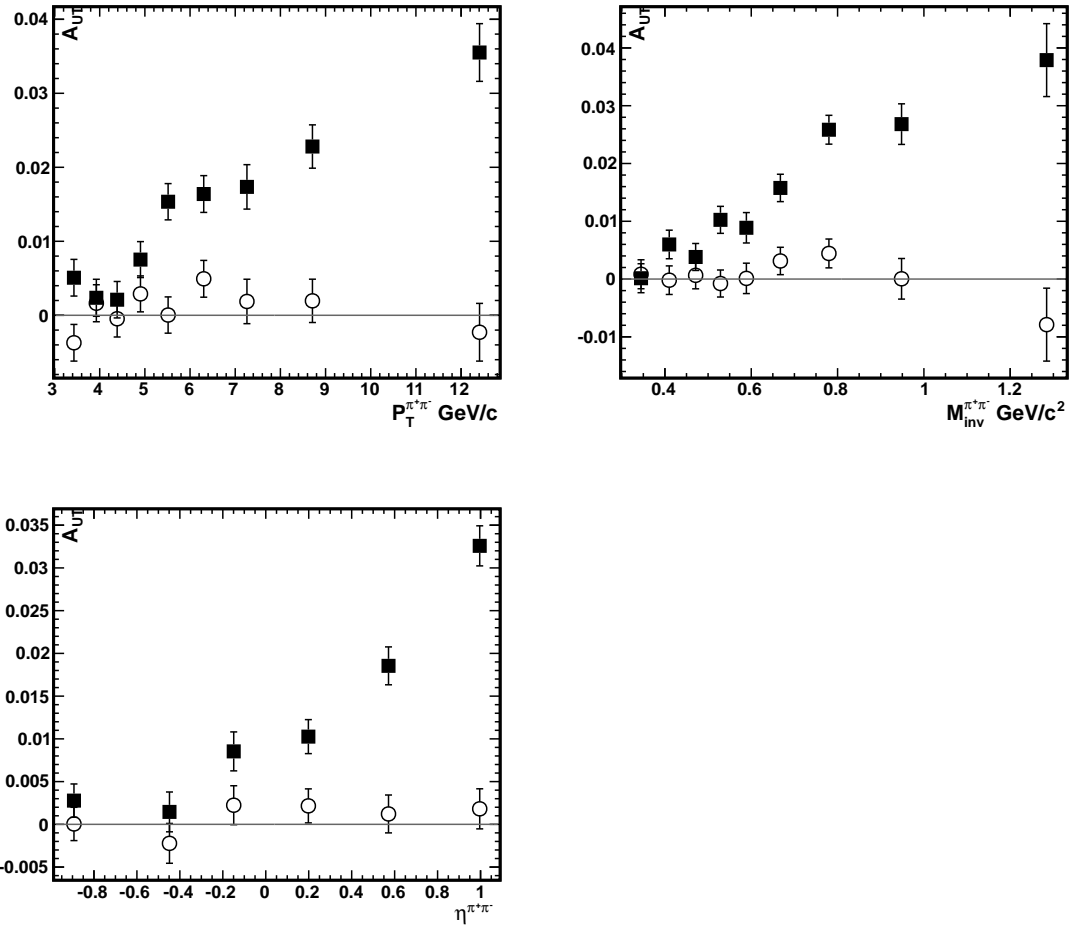


Figure 7.3: Randomly assigned spin state (open circles) show no sign of asymmetry in any kinematic variable. Correct assignment (solid squares) shown for comparison.  
 $-2 < \eta^{\pi^+\pi^-} < 2$  for  $P_T^{\pi^+\pi^-}$  and  $M_{inv}^{\pi^+\pi^-}$  plots.

### **7.3 Two Dimensional Kinematic Binning**

We were lucky enough to get a much larger data set in 2012. This enabled us to not only break each kinematic variable up into more bins but also bin in multiple kinematic variables at once. This is ideal for extracting the transversity distribution.

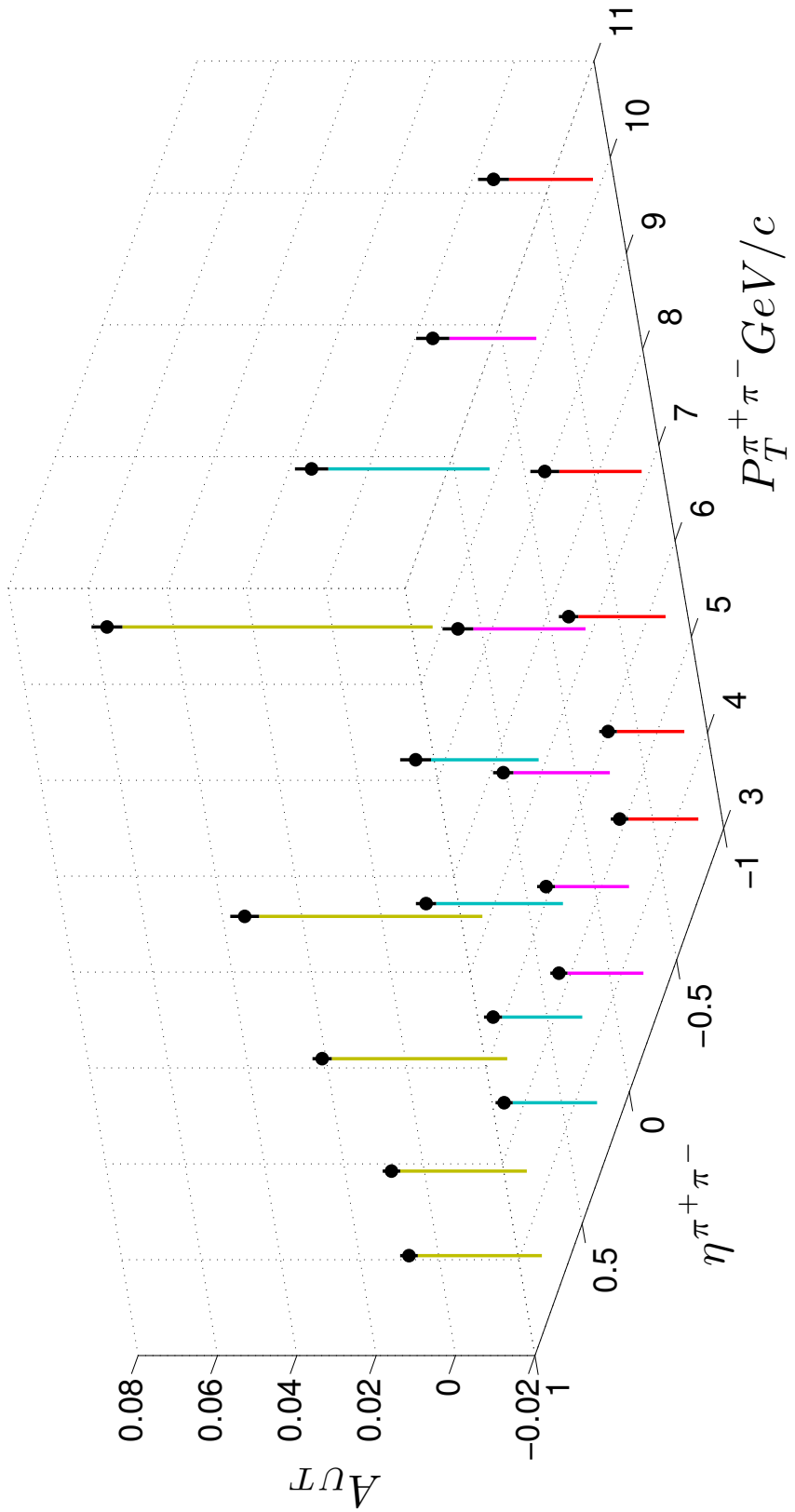
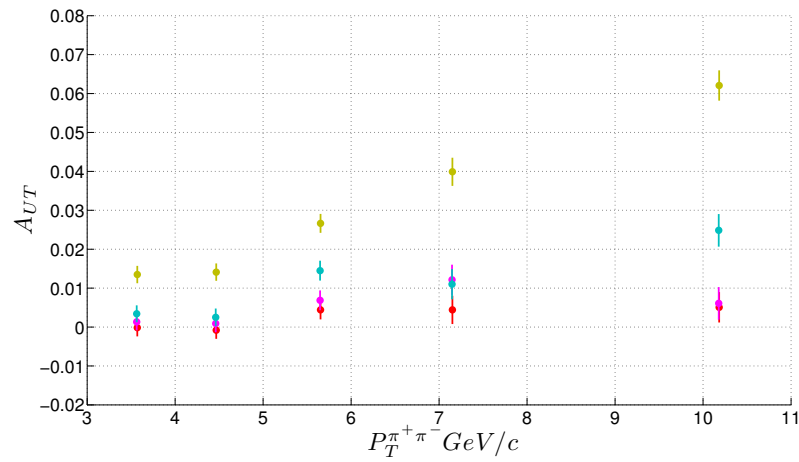
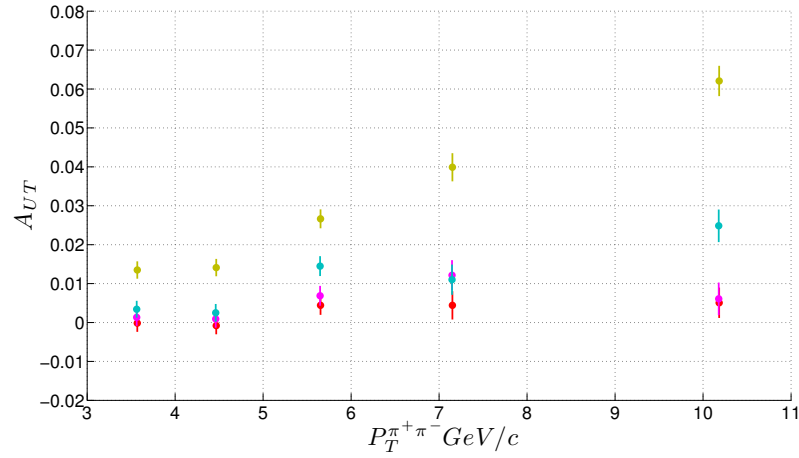


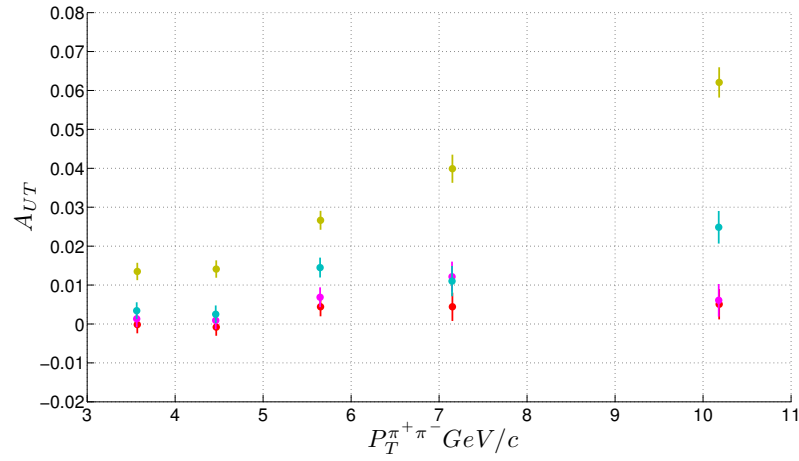
Figure 7.4:  $A_{UT}$  versus  $P_T^{\pi^+\pi^-}$  and  $\eta^{\pi^+\pi^-}$ . Different colored stands denote different  $\eta^{\pi^+\pi^-}$  bins. Note zero is not ground level of the plot.



(a)



(b)



(c)

Figure 7.5: Different views of 7.4 for more precise viewing.

(a) view of the XY plane. (b) view of ..... (c) view of .....

## 7.4 Kaon Pion Pairs

$K\pi$  pairs go through an intermediate vector meson  $K^*(892)$ . The IFF should be enhanced in this range just like in the  $\rho$  mass range for  $\pi^+\pi^-$  pairs. ||||| Do I go into finding the  $K\pi$  pairs here in the results chapter or do I make a section in part 6 for finding  $K\pi$  pairs like I have for  $\pi\pi$  pairs??|||||

Detecting pions was simple because there are so many more pions than kaons or protons. We attempt to cut as many kaons and pions out as possible and the rest just come as a dilution to the proton sample. It is a lot more difficult to specifically look for kaons. To do this we have to use the ToF as well as the ionization energy loss in the TPC to distinguish between pions and kaons accurately. Figure 7.6 shows a heat map of the particle mass determined by the ToF vs the track  $n_\sigma(\pi)$  determined by the ionization energy loss. This is separated into 11 different track momentum ranges. Looking at the first momentum range in the upper left hand plot, the protons are seen as the faint green region at an time of flight mass of just under one  $\text{GeV}/c^2$ . As expected the pions are located around the bright red region at centered at  $n_\sigma(\pi) = 0$ . The kaons are the faint green region just above and to the left of the pion region. Since protons are so far away from kaons and pions, they are easily removed from the sample with a ToF mass cut. However in order to correctly identify kaons, we need to make a distinction between them and pions.

Looking at each momentum bin individually I constructed the interface between the pion region and the kaon region. I then removed the overlap region where it was impossible to distinguish pions and kaons. This can be seen for the lowest momentum bin in figure ???. Everything between the white lines is not included in the analysis. Particles above the top line is taken to be a kaon, except for the clear proton region which is removed by a horizontal ToF mass cut. Everything below the bottom line is declared a pion. I was

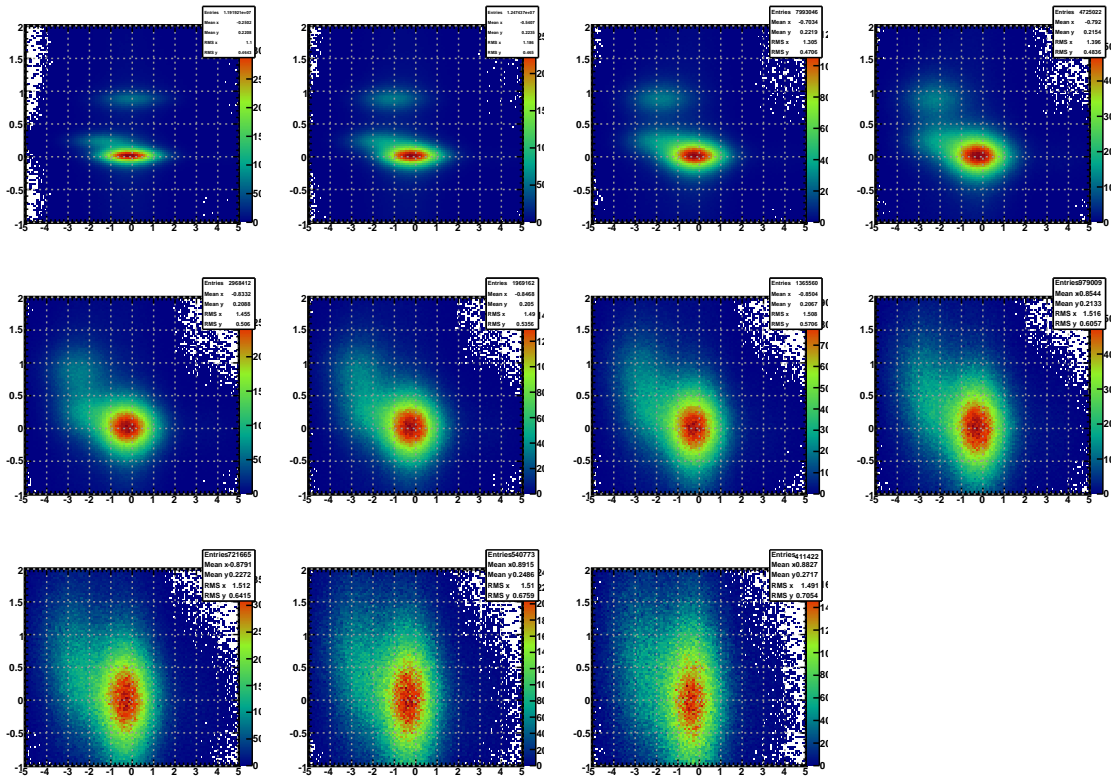


Figure 7.6

able to do this method with varying success for the first 4 momentum bins. The pion, kaon, and sometimes even proton regions in the remaining bins overlapped too much and were not included in the analysis. As the track momentum increases the exclusion region between the white lines increases.

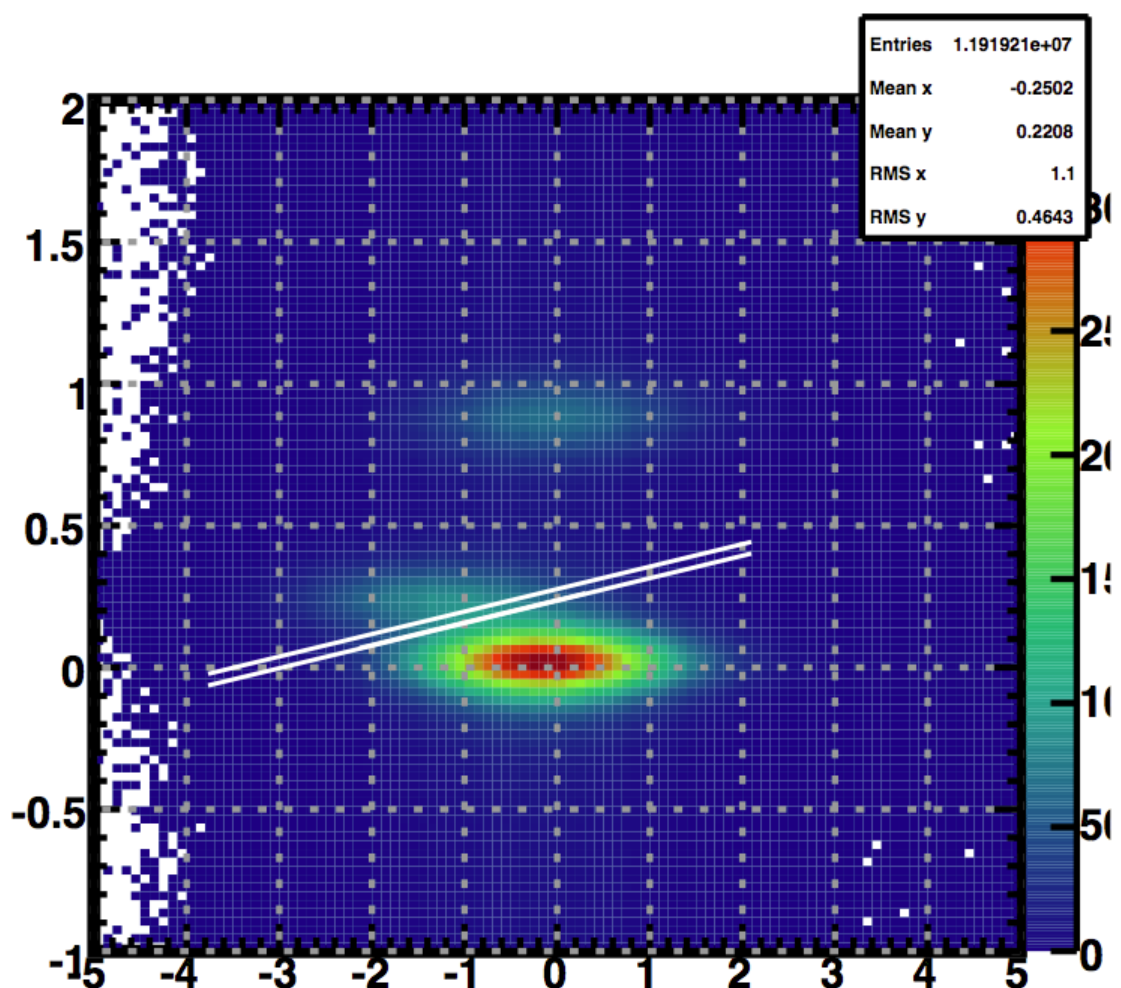


Figure 7.7

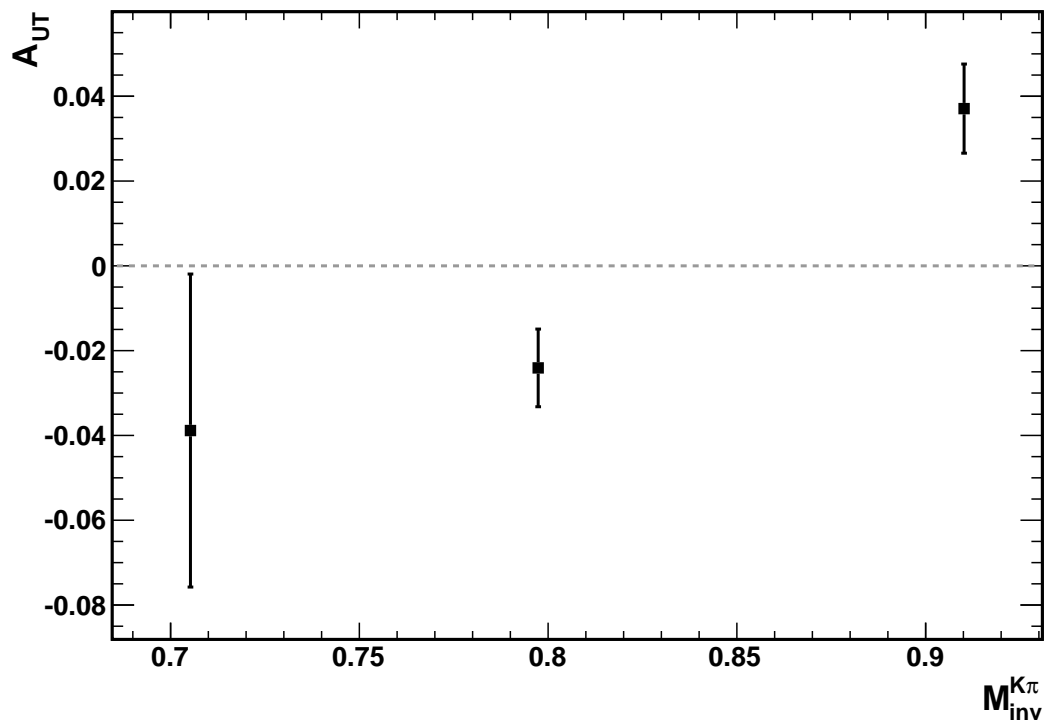


Figure 7.8: Asymmetry vs Invariant Mass for Kaon Pion Pairs. Nonzero asymmetry is only seen in the mass bin containing the  $K^*(892)$  mass.

## 8 Trigger Bias

The way the STAR triggers select events introduces a bias to our sample. The main triggers I use in my analysis are the barrel jet patch triggers and the barrel high tower triggers. These triggers are fired when there is substantial amount of energy deposited in one or a group of towers. This happens when there are a lot of high energy neutral particles in the event.

The trigger also has a bias toward events coming from a quark carrying a high momentum fraction  $x$ . A quark with a large  $x$  will lead to outgoing products carrying more energy. These products will have a greater chance to be over the trigger threshold.

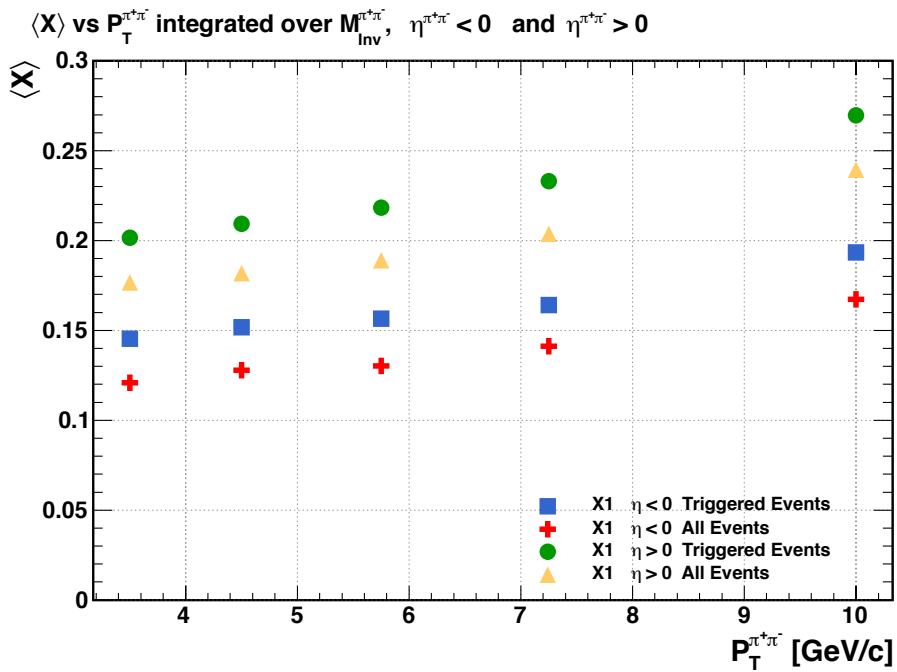


Figure 8.1: The average momentum fraction  $x$  of the polarized quark (quark 1) is larger for triggered events than for all events. This effect is seen if both the forward and backward directions and for all  $\pi^+\pi^-$  transverse momenta. Note this figure is from the 2006 set up

## **9 discussion**

testing bibliography [10][2][5][15][6][4][7][1][12][9][8][13]

## Bibliography

- [1] K.H. Ackermann et al. “STAR detector overview”. In: *Nuclear Instruments and Methods in Physics Research A* 499 (2003), pp. 624–632. URL: [http://dx.doi.org/10.1016/S0168-9002\(02\)01960-5](http://dx.doi.org/10.1016/S0168-9002(02)01960-5).
- [2] A. Airapetian et al. “Measurement of the Proton Spin Structure Function  $g_1^p$  with a Pure Hydrogen Target”. In: *Phys.Lett.B* 442 (1998), pp. 484–492. URL: <http://arxiv.org/abs/hep-ex/9807015v1>.
- [3] Marco Radici Alessandro Bacchetta. “Dihadron interference fragmentation functions in proton-proton collisions”. In: *Phys. Rev. D* 70 (3 2004). URL: DOI : 10.1103/PhysRevD.70.094032.
- [4] M. Anderson et al. “The STAR time projection chamber: a unique tool for studying high multiplicity events at RHIC”. In: *Nuclear Instruments and Methods in Physics Research A* 499 (2003), pp. 659–678. URL: <http://arxiv.org/abs/nucl-ex/0301015>.
- [5] Marco Radici Aurore Courtoy Alessandro Bacchetta and Andrea Bianconi. “First extraction of Interference Fragmentation Functions from  $e^+e^-$  data”. In: *Phys.Rev.D* 85 (2012). URL: <http://arxiv.org/abs/1202.0323>.

- [6] M. Beddoa et al. “The STAR Barrel Electromagnetic Calorimeter”. In: *Nuclear Instruments and Methods in Physics Research A* 499 (2003), pp. 725–739. URL: [http://dx.doi.org/10.1016/S0168-9002\(02\)01970-8](http://dx.doi.org/10.1016/S0168-9002(02)01970-8).
- [7] F. Bergsmaa et al. “The STAR detector magnet subsystem”. In: *Nuclear Instruments and Methods in Physics Research A* 499 (2003), pp. 633–639. URL: [http://dx.doi.org/10.1016/S0168-9002\(02\)01961-7](http://dx.doi.org/10.1016/S0168-9002(02)01961-7).
- [8] HERMES Collaboration. “Evidence for a transverse single-spin asymmetry in lepto-production of  $\pi^+\pi^-$  pairs”. In: *Journal of High Energy Physics* 0806 (2008), p. 017. URL: <http://arxiv.org/abs/0803.2367>.
- [9] The COMPASS Collaboration. “Transverse spin effects in hadron-pair production from semi-inclusive deep inelastic scattering”. In: *Phys. Lett. B* 713 (2012), pp. 10–16. URL: <http://arxiv.org/abs/1202.6150>.
- [10] I.Alekseev et al. “Polarized proton collider at RHIC”. In: *Nuclear Instruments and Methods in Physics Research A* 499 (2003), pp. 392–414. URL: [http://dx.doi.org/10.1016/S0168-9002\(02\)01946-0](http://dx.doi.org/10.1016/S0168-9002(02)01946-0).
- [11] W.J. Llope et al. “The TOFp/pVPD time-of-flight system for STAR”. In: *Nuclear Instruments and Methods in Physics Research A* 522 (3 2004), pp. 252–273. URL: <doi:10.1016/j.nima.2003.11.414>.
- [12] S. Ozaki M. Harrison T. Ludlam. “RHIC project overview”. In: *Nuclear Instruments and Methods in Physics Research A* 499 (2003), pp. 235–244. URL: [http://dx.doi.org/10.1016/S0168-9002\(02\)01937-X](http://dx.doi.org/10.1016/S0168-9002(02)01937-X).
- [13] Gerald G. Ohlsen and P.W. Keaton Jr. “Techniques for Measurement of spin- $\frac{1}{2}$  and spin-1 Polarization Analyzing Tensors”. In: *Nuclear Instruments and Methods* 109 (1973), pp. 41–59.

- [14] Jian Tang. “Probing the Nucleon’s Transversity Via Two-Meson Production in Polarized Nucleon-Nucleon Collisions”. In: *Submitted to Phys. Rev. D* (1998). URL: [arXiv:hep-ph/9807560](https://arxiv.org/abs/hep-ph/9807560).
- [15] A. Vossen et al. “Observation of Transverse Polarization Asymmetries of Charged Pion Pairs in  $e^+e^-$  Annihilation near  $\sqrt{s} = 10.58$  GeV”. In: *Phys. Rev. Lett.* 107 (7 2011), p. 072004. DOI: 10.1103/PhysRevLett.107.072004. URL: <http://arxiv.org/abs/1104.2425>.